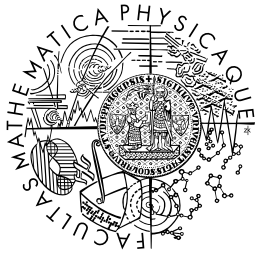

FACULTY
OF MATHEMATICS
AND PHYSICS
Charles University

MASTER THESIS

Jan Šenk

Model of coherent electron dynamics in molecules

Institute of Theoretical Physics

Supervisor of the master thesis: doc. RNDr. Přemysl Kolorenč, Ph.D.
Study programme: Physics
Study branch: Theoretical Physics

Prague 2023

I declare that I carried out this master thesis independently, and only with the cited sources, literature and other professional sources. It has not been used to obtain another or the same degree.

I understand that my work relates to the rights and obligations under the Act No. 121/2000 Sb., the Copyright Act, as amended, in particular the fact that the Charles University has the right to conclude a license agreement on the use of this work as a school work pursuant to Section 60 subsection 1 of the Copyright Act.

In Prague, May 4, 2023 .....

Author's signature

I want to thank my supervisor, doc. Přemysl Kolorenč, for his patient guidance and valuable advice. My thanks also go to my parents, who supported me on the journey throughout my studies, never ceasing to believe that I would succeed.

Title: Model of coherent electron dynamics in molecules

Author: Jan Šenk

Institute: Institute of Theoretical Physics

Supervisor: doc. RNDr. Přemysl Kolorenč, Ph.D., Institute of Theoretical Physics

Abstract: An ultrashort laser pulse photoionizing the molecule produces a superposition of a few cationic states. The coupling between the electrons and the nuclei has been predicted to cause fast decoherence. In this thesis, a two-dimensional model of coupled electron-nuclear dynamics in molecules is constructed. It is based on a harmonic potential in the nuclear degree of freedom and a double harmonic potential representing two centers that bind the electrons. The electronic potential's dependence on the nuclear configuration facilitates the coupling. Thanks to the simplicity of the model, it is numerically exactly solvable. We use the basis of its eigenstates to calculate the evolution of any initial state. Several quantities are used to measure decoherence and unravel the underlying mechanisms. Especially useful is the Wigner quasiprobability distribution. A few fundamental cases of the model are analyzed, and it is used to approximate the coherence dynamics in the normal modes of the H_2O^+ cation.

Keywords: coherence, decoherence, density matrix, electron dynamics, vibrational dynamics.

Contents

Introduction

In this thesis, we construct a simple model of coherent electron dynamics in molecules, mainly focusing on the process of its decoherence. Exposing a molecule to an ultrashort laser pulse that ionizes it leads to a superposition of several cationic states. This process is called *photoionization*. Under certain conditions, the coherence manifests itself in the oscillation of physical quantities, e.g., the *charge density* – this phenomenon is called *charge migration*. The energies of the electronic states depend on the configuration of the molecule, and this dependence is different for the individual states. This coupling of the electronic state to the configuration of the nuclei leads to different nuclear wave packet dynamics in each electronic state, which causes electronic decoherence – the initially coherent superposition transforms into an incoherent mixture.

In the first chapter, we discuss the phenomena we want to reproduce in our model. We describe the coherent electron dynamics and the impact of nuclear dynamics in the simplest possible terms. Two fundamentally different approaches to separating the molecular system into its electronic and nuclear parts are compared. We describe three mechanisms of decoherence and introduce the quantities that can be used to quantify it. We then comment on the photoionization process itself and the importance of the ultrashort timescale of the laser pulses in producing the coherent superpositions.

The second chapter describes our model of the coupled electron-nuclear dynamics and the approach to solving it. Our two-dimensional model comprises a harmonic potential well in the "nuclear coordinate" and a combination of two such wells in the "electronic coordinate", with parameters depending on the nuclear configuration. We use a specific basis to evaluate the matrix elements of all relevant operators and find the system's eigenstates via the diagonalization of the complete Hamiltonian. This allows us to evolve the system from its initial state to an arbitrary time.

The center point of this thesis is the third chapter, with our results and their discussion. This chapter is divided into three parts. In the first part, we verify that our model yields coherent electronic behaviour in the case of uncoupled electron and nuclear dynamics. Then, we present three primary cases of coupled electron-nuclear dynamics defined by different parameters of the electronic potential depending on the nuclear coordinate. We use the geometric and momentum overlap of the nuclear wave packets to interpret the decoherence. We find the Wigner quasiprobability distribution to be a helpful tool. In the final part, we apply the model to approximate the evolution of a superposition of states of an H_2O^+ cation.

Unless specified otherwise, we use the *Hartree atomic units* throughout this thesis. These are defined by the following physical constants being dimensionless and their numerical value being 1: *reduced Planck constant* $\hbar$, *elementary charge* e, *Bohr radius* a_0, and *electron rest mass* m_e.

1. Theory

1.1 Coherent electron dynamics in atoms

This first section presents the general theory of coherent electron dynamics in atoms (and in molecules in the approximation of fixed nuclei). We will follow the approach from [1].

Let $\hat{H}_\mathrm{e}$ be the Hamiltonian for the electronic system and let $|\psi_i\rangle$ be its eigenstates with corresponding eigenenergies E_i. The evolution of the state of the system $|\Psi(t)\rangle$ is given by the time-dependent Schrödinger equation [2, p. 223]

$$i\frac{\mathrm{d}}{\mathrm{d}t}|\Psi(t)\rangle = \hat{H}_\mathrm{e}|\Psi(t)\rangle\,, \tag{1.1}$$

with the initial condition

$$|\Psi(t=0)\rangle = |\Psi_0\rangle\,. \tag{1.2}$$

We can express the initial state of the system as a linear combination of the eigenstates of the Hamiltonian

$$|\Psi_0\rangle = \sum_i \alpha_i |\psi_i\rangle\,, \quad \sum_i |\alpha_i|^2 = 1. \tag{1.3}$$

The second equality is the consequence of the usual normalization $\langle\Psi_0|\Psi_0\rangle = 1$ and orthonormality of the eigenbasis. Thanks to the Hamiltonian $\hat{H}_\mathrm{e}$ being time-independent, we can integrate the equation (1.1), obtaining

$$|\Psi(t)\rangle = \sum_i \alpha_i \mathrm{e}^{-iE_it}|\psi_i\rangle\,. \tag{1.4}$$

We can trivially see that the populations P_i of the individual eigenstates do not change,

$$P_i = |\langle\psi_i|\Psi(t)\rangle|^2 = |\alpha_i|^2. \tag{1.5}$$

Now, we want to proceed to calculate the time-dependent electronic density corresponding to the evolution of the state $|\Psi(t)\rangle$. In an atom with N electrons, we have a collection of N three-dimensional coordinate spaces describing the position of all the electrons. We can integrate over $3N-3$ of the coordinates and obtain a density in a single three-dimensional space. Let us denote r a coordinate in this space and $\boldsymbol{r}$ the collection of N such coordinates. The electronic density is defined as

$$\rho(r,t) = \int \mathrm{d}^{N-1}r\,|\langle\boldsymbol{r}|\Psi(t)\rangle|^2. \tag{1.6}$$

This can be manipulated into the following form:

$$\rho(r,t) = \mathrm{Tr}\Big(\hat{\rho}(t)\hat{T}(r)\Big), \tag{1.7}$$

$$\hat{\rho}(t) = |\Psi(t)\rangle\langle\Psi(t)|\,, \tag{1.8}$$

$$\hat{T}(r) = \int \mathrm{d}^{N-1}r\,|\boldsymbol{r}\rangle\langle\boldsymbol{r}|\,, \tag{1.9}$$

where $\hat{\rho}(t)$ is the density operator (see ,e.g., [2, Complement $\mathrm{E_{III}}$]) corresponding to the state of the system and $\hat{T}(r)$ is the reduced transition density operator. We can write the three above expressions in the basis of eigenstates of the Hamiltonian as follows:

$$\rho(r,t) = \sum_{ij} \rho_{ij}(t) T_{ji}(r), \tag{1.10}$$

$$\rho_{ij}(t) \equiv \langle \psi_i | \Psi(t) \rangle \langle \Psi(t) | \psi_j \rangle = \alpha_i \alpha_j^* \mathrm{e}^{-i(E_i - E_j)t}, \tag{1.11}$$

$$T_{ji}(r) \equiv \int \mathrm{d}^{N-1} r \, \langle \psi_j | \boldsymbol{r} \rangle \langle \boldsymbol{r} | \psi_i \rangle = \int \mathrm{d}^{N-1} r \, \psi_j^*(\boldsymbol{r}) \psi_i(\boldsymbol{r}). \tag{1.12}$$

The density matrix $\rho_{ij}(t)$ contains information about the evolution of the system and is constructed from the coefficients of the initial superposition (1.3) and the energies of the eigenstates. The transition density $T_{ji}(r)$ contains information on the spatial distribution of the electronic density and is constructed from the coordinate representation of the eigenstates. We usually choose the (bound) eigenstates to be real functions in the coordinate representation, making the transition density matrix elements real. We can rewrite the electronic density one more time in a form more suitable for the analysis of the properties of the evolution,

$$\rho(r,t) = \sum_i |\alpha_i|^2 T_{ii}(r) + 2 \sum_{i>j} |\alpha_i| |\alpha_j| \cos(\Delta E_{ij} t + \Delta \varphi_{ij}) T_{ij}(r), \tag{1.13}$$

where we denoted

$$\Delta E_{ij} = E_i - E_j, \quad \Delta \varphi_{ij} = \varphi_j - \varphi_i, \quad \alpha_i = |\alpha_i| \mathrm{e}^{i\varphi_i}.$$

The second term of the expression on the right side of (1.13) contains the non-trivial part of the evolution. It consists of the transition density $T_{ij}(r)$ and a time-dependent prefactor – the sum of the two corresponding off-diagonal elements of the density matrix, that we denote

$$C_{ij}(t) \equiv \rho_{ij}(t) + \rho_{ji}(t) = 2|\alpha_i||\alpha_j| \cos(\Delta E_{ij} t + \Delta \varphi_{ij}) \tag{1.14}$$

and call *electronic coherence* between the i-th and j-th eigenstate.

For simplicity, we can now think of the case where only two eigenstates are present in the initial superposition

$$P_i = 0, \quad i = 3, \ldots \tag{1.15}$$

The coherence manifests itself in the cosine oscillatory behaviour of the evolution of the electronic density. Angular frequency is given by (in other than atomic units proportional to) the difference of the energies of the two considered eigenstates. Two conditions have to be met for these oscillations to be present. The two populated eigenstates have to have different energies, and both eigenstates must have non-zero populations. There is one additional condition for the oscillations to be visible – the relevant transition density matrix element must be non-zero.

1.2 The density operator formalism in the context of molecules

Let us take a step aside and summarize the basics of solving the molecular problem. We denote $\boldsymbol{R}$ the collection of the coordinates of the nuclei. The system is described by a molecular Hamiltonian in the following form (see, e.g., [3])

$$\begin{aligned}\hat{H}(\boldsymbol{r},\boldsymbol{R}) &= \hat{T}_{\mathrm{N}}(\boldsymbol{R}) + \hat{H}_{\mathrm{e}}(\boldsymbol{r},\boldsymbol{R}) \\ &= \hat{T}_{\mathrm{N}}(\boldsymbol{R}) + \hat{T}_{\mathrm{e}}(\boldsymbol{r}) + \hat{V}_{\mathrm{e-e}}(\boldsymbol{r}) + \hat{V}_{\mathrm{N-e}}(\boldsymbol{r},\boldsymbol{R}) + \hat{V}_{\mathrm{N-N}}(\boldsymbol{R}),\end{aligned} \tag{1.16}$$

where $\hat{T}_{\mathrm{N}}$ is the kinetic energy operator of the nuclei and $\hat{H}_{\mathrm{e}}$ is the electronic Hamiltonian consisting of the kinetic energy operator of the electrons $\hat{T}_{\mathrm{e}}$ and the potentials of the interactions between two electrons $\hat{V}_{\mathrm{e-e}}$, an electron and a nucleus $\hat{V}_{\mathrm{N-e}}$, and two nuclei $\hat{V}_{\mathrm{N-N}}$. The last term is sometimes not included in the electronic Hamiltonian. In order to solve the time-dependent Schrödinger equation generated by this Hamiltonian, we usually start by finding the eigenstates of the electronic Hamiltonian

$$\hat{H}_{\mathrm{e}}(\boldsymbol{r};\boldsymbol{R})\psi_i(\boldsymbol{r};\boldsymbol{R}) = E_i(\boldsymbol{R})\psi_i(\boldsymbol{r};\boldsymbol{R}), \tag{1.17}$$

where we used the coordinate representation. The electronic time-independent Schrödinger equation is solved with respect to the electronic variables $\boldsymbol{r}$ and is parametrized by the nuclear configuration $\boldsymbol{R}$, which is denoted by the semicolon. These $\boldsymbol{r}$- and $\boldsymbol{R}$-dependent electronic states are called *adiabatic states*, and the $\boldsymbol{R}$-dependent energies are called *adiabatic potential energy surfaces* (PESs).

In terms of these states, the complete time-dependent wave function can be written as

$$\Phi(\boldsymbol{r},\boldsymbol{R},t) = \sum_i \chi_i(\boldsymbol{R},t)\psi_i(\boldsymbol{r};\boldsymbol{R}), \tag{1.18}$$

where the functions $\chi(\boldsymbol{R},t)$ are called *nuclear wave packets* and the expansion is called *adiabatic representation*. The adiabatic states are coupled together and with the nuclear wave packets via the nuclear kinetic energy operator. When the PESs corresponding to two given electronic states are not very close to each other at the geometry where their nuclear wave packets are non-zero, the equation for the nuclear wave packets decouples and yields

$$i\frac{\partial}{\partial t}\chi_i(\boldsymbol{R},t) = \left(\hat{T}_{\mathrm{N}}(\boldsymbol{R}) + E_i(\boldsymbol{R})\right)\chi_i(\boldsymbol{R},t). \tag{1.19}$$

This is called the *Born-Oppenheimer*[1] *approximation*.

This approximation breaks down in the vicinity of the so-called conical intersections (CIs) and avoided crossings, and the equations for the corresponding $\chi_i(\boldsymbol{R},t)$ become coupled. In such a case, one can perform the so-called *diabatic transformation*. It essentially transforms the (usually two) coupled electronic adiabatic states with an $\boldsymbol{R}$-dependent unitary transformation so that the resulting

[1]Strictly speaking, it is the *adiabatic Born-Oppenheimer approximation* because we neglected all electronic matrix elements of the nuclear kinetic energy operator, $\langle\psi_i(\boldsymbol{r};\boldsymbol{R})|\hat{T}_{\mathrm{N}}(\boldsymbol{R})|\psi_j(\boldsymbol{r};\boldsymbol{R})\rangle = 0$, $\forall i,j$. In the *Born-Oppenheimer approximation*, only the off-diagonal terms, $i \neq j$, are neglected.

states diagonalize the nuclear kinetic energy operator. The coupling is transferred into additional potential energy terms.

Alternatively, we can solve the electronic eigenproblem (1.17) for one fixed geometry $\boldsymbol{R}_0$ and use the resulting $\boldsymbol{R}$-independent functions for expansion of the full time-dependent wave function

$$\Phi(\boldsymbol{r}, \boldsymbol{R}, t) = \sum_i \tilde{\chi}_i(\boldsymbol{R}, t)\psi_i(\boldsymbol{r}; \boldsymbol{R}_0). \tag{1.20}$$

This is called the *strictly diabatic representation*, and the states $\psi_i(\boldsymbol{r}; \boldsymbol{R}_0)$ are called *strictly diabatic states*. The dynamic equation for the corresponding nuclear wave packet is

$$i\frac{\partial}{\partial t}\tilde{\chi}_i(\boldsymbol{R}, t) = \left(\hat{T}_{\mathrm{N}}(\boldsymbol{R}) + \sum_i W_{ij}(\boldsymbol{R})\right)\tilde{\chi}_i(\boldsymbol{R}, t), \tag{1.21}$$

where

$$W_{ij}(\boldsymbol{R}) = \int \mathrm{d}\boldsymbol{r}\, \psi_j^*(\boldsymbol{r}; \boldsymbol{R}_0)\hat{H}_{\mathrm{e}}(\boldsymbol{r}, \boldsymbol{R})\psi_i(\boldsymbol{r}; \boldsymbol{R}_0). \tag{1.22}$$

The equations for various $\tilde{\chi}_i(\boldsymbol{R})$ are therefore inherently coupled. We have not used the Born-Oppenheimer approximation, nor would it help us. The equations are strictly decoupled only at the geometry $\boldsymbol{R}_0$. The diagonal elements of the W matrix are called the *diabatic potential energy surfaces*.

Let us repeat once more the two representations introduced above and rewrite them in the abstract Dirac formalism,

$$\Phi(\boldsymbol{r}, \boldsymbol{R}, t) = \sum_i \chi_i(\boldsymbol{R}, t)\psi_i(\boldsymbol{r}; \boldsymbol{R}) \qquad \longleftrightarrow \quad |\Phi(t)\rangle = \sum_i |\chi_i(t)\rangle\, |\psi_i\rangle\,, \tag{1.23}$$

$$\Phi(\boldsymbol{r}, \boldsymbol{R}, t) = \sum_i \tilde{\chi}_i(\boldsymbol{R}, t)\psi_i(\boldsymbol{r}; \boldsymbol{R}_0) \qquad \longleftrightarrow \quad |\Phi(t)\rangle = \sum_i |\tilde{\chi}_i(t)\rangle\, |\tilde{\psi}_i\rangle\,. \tag{1.24}$$

This shows that using these two representations, we have two different *separations* of the molecule to electronic and nuclear subsystems. Of course, the strictly diabatic states $\psi_i(\boldsymbol{r}; \boldsymbol{R}_0)$ are probably not physically relevant. On the other hand, the diabatic states generated by the diabatic transformation are useful – they are similar to the adiabatic ones when far from an avoided crossing and in the region of avoided crossings often provide more intuitive picture of the dynamical evolution.

When we construct electronic or nuclear observables, we must remember that they will be different in these two separations. For example, if we want to construct electronic/nuclear densities by integrating over all nuclear/electronic coordinates and all but one electronic/nuclear coordinates, this corresponds to the diabatic separation. In general, if we want to work in the coordinate representation and the adiabatic separation, the purely electronic quantities will be geometry-dependent.

To illustrate the discussed nuances, let us present the electronic density in four different cases – two different separations and two different definitions of the quantity. The results are gathered in Table 1.1. We can see that for diabatic separation, both definitions of the electronic density (cases A and B) yield the same result. This happens because, in diabatic separation, the electronic subsystem is

given by functions of only electronic coordinates, and the nuclear subsystem comprises functions of only nuclear coordinates. For adiabatic separation, the results differ. When we sum over the basis of the nuclear subsystem (case D), we obtain $\boldsymbol{R}$-dependent electronic density. In all but case C, we can interpret the result as a trace of a product of two matrices, where the matrix given by the integral over $\boldsymbol{R}$ is the reduced electronic density matrix (defined below in (1.28)) of the system and the matrix given by the integral over all but one electronic coordinates is an observable on the electronic subsystem. Therefore, we have a form of (1.10) in these three cases – an analogy to the fixed nuclei case. In case C, however, the integral over $\boldsymbol{R}$ spans the whole formula, and we cannot interpret it as a partial trace of the density operator. The whole formula does not represent a trace of a product of two matrices.

Table 1.1: The four discussed cases of the separation of the molecular system and the definition of electronic density.

Definition \ Separation	Diabatic	Adiabatic
$\int \mathrm{d}^{N-1}r \int \mathrm{d}\boldsymbol{R}$	Case A	Case C
$\int \mathrm{d}^{N-1}r \sum_{\text{nuc.bas.}}$	Case B	Case D

$$\rho^{\mathrm{A}}(r,t) = \sum_{ij} \left(\int \mathrm{d}\boldsymbol{R}\, \tilde{\chi}_i(\boldsymbol{R},t)\tilde{\chi}_j^*(\boldsymbol{R},t) \right) \left(\int \mathrm{d}^{N-1}r\, \psi_i(\boldsymbol{r},\boldsymbol{R}_0)\psi_j^*(\boldsymbol{r},\boldsymbol{R}_0) \right)$$

$$\rho^{\mathrm{B}}(r,t) = \sum_{ij} \left(\int \mathrm{d}\boldsymbol{R}\, \tilde{\chi}_i(\boldsymbol{R},t)\tilde{\chi}_j^*(\boldsymbol{R},t) \right) \left(\int \mathrm{d}^{N-1}r\, \psi_i(\boldsymbol{r},\boldsymbol{R}_0)\psi_j^*(\boldsymbol{r},\boldsymbol{R}_0) \right)$$

$$\rho^{\mathrm{C}}(r,t) = \sum_{ij} \left(\int \mathrm{d}\boldsymbol{R}\, \chi_i(\boldsymbol{R},t)\chi_j^*(\boldsymbol{R},t) \int \mathrm{d}^{N-1}r\, \psi_i(\boldsymbol{r},\boldsymbol{R})\psi_j^*(\boldsymbol{r},\boldsymbol{R}) \right)$$

$$\rho^{\mathrm{D}}(r,\boldsymbol{R},t) = \sum_{ij} \left(\int \mathrm{d}\boldsymbol{R}\, \chi_i(\boldsymbol{R},t)\chi_j^*(\boldsymbol{R},t) \right) \left(\int \mathrm{d}^{N-1}r\, \psi_i(\boldsymbol{r},\boldsymbol{R})\psi_j^*(\boldsymbol{r},\boldsymbol{R}) \right)$$

Which of these pictures is correct is not apparent, and various groups studying the electronic decoherence effect choose different approaches. For example, in Refs. [4] or [5], the diabatic separation is used. More specifically, the strictly diabatic states are used in the former, and the general diabatic states in the latter. The authors of Ref. [6] use the adiabatic separation and the definition of electronic quantities through the sum over the basis of the nuclear subsystem, making them $\boldsymbol{R}$-dependent. Then they argue that if their electronic operator and the adiabatic states depend only weakly on the nuclear coordinates, they approximately obtain the separation and $\boldsymbol{R}$-independence as in the case of diabatic separation. Finally, the authors of Ref. [1], the book we followed in the first section, use the adiabatic separation and then, incorrectly or at least with not explicitly mentioned approximations, calculate the electronic density as a trace of a product of the reduced electronic density matrix and the $\boldsymbol{R}$-independent electronic transition density.

1.3 Mechanisms of decoherence

After the detour in the previous section, we shall return to the introduction of Ref. [1], albeit in a more general sense than presented in the book. Let us suppose that the evolution of the state of the system is described in the abstract formalism as

$$|\Phi(t)\rangle = \sum_i |\chi_i(t)\rangle\, |\psi_i\rangle\,, \tag{1.25}$$

where $\{|\psi_i\rangle\}$ is the electronic basis whose exact character (i.e., adiabatic or diabatic) we do not specify, and $\{|\chi_i(t)\rangle\}$ are the corresponding nuclear wave packets. We shall investigate the evolution of the expectation value of an arbitrary electronic observable $\hat{A}_\mathrm{e}$. Using once again the density operator formalism, we obtain the following:

$$A_\mathrm{e}(t) \equiv \langle A_\mathrm{e}(t)\rangle = \mathrm{Tr}\Big(\hat{\rho}(t)\hat{A}_\mathrm{e}\Big) = \mathrm{Tr}\Big(\hat{\rho}_\mathrm{e}(t)\hat{A}_\mathrm{e}\Big), \tag{1.26}$$

$$\hat{\rho}(t) = |\Phi(t)\rangle\, \langle\Phi(t)|\,, \tag{1.27}$$

$$\hat{\rho}_\mathrm{e} = \mathrm{Tr}_\mathrm{N}(\hat{\rho}(t)), \tag{1.28}$$

where the last equality defines the electronic reduced density operator as a partial trace over the nuclear subsystem denoted by Tr_N. Similarly to the first section, we can express the operators as matrices in the electronic basis representation:

$$A_\mathrm{e}(t) = \sum_{ij} \rho_{\mathrm{e},ij}(t) A_{\mathrm{e},ji}, \tag{1.29}$$

$$\rho_{\mathrm{e},ij}(t) = \langle\chi_j(t)|\chi_i(t)\rangle\,, \tag{1.30}$$

$$A_{\mathrm{e},ji} = \langle\psi_j|\hat{A}_\mathrm{e}|\psi_i\rangle\,. \tag{1.31}$$

Let us assume that the matrix elements $A_{\mathrm{e},ij}$ are real. Again, we usually choose the electronic basis to consist of real functions in the coordinate representation, making our assumption valid for any electronic operator $\hat{A}_\mathrm{e}$ that can be written as a function of the position operator and even powers of the momentum operator. We can then rewrite the evolution of the expectation value in a form analogous to (1.13),

$$A_\mathrm{e}(t) = \sum_i \langle\chi_i(t)|\chi_i(t)\rangle\, A_{\mathrm{e},ii} + 2\sum_{i>j} \mathrm{Re}(\langle\chi_i(t)|\chi_j(t)\rangle) A_{\mathrm{e},ij}. \tag{1.32}$$

In this case, the coherence between any two states reads

$$C_{ij}(t) = 2\,\mathrm{Re}(\langle\chi_i(t)|\chi_j(t)\rangle), \tag{1.33}$$

and the populations of the electronic states are time-dependent,

$$P_i(t) = |\langle\psi_i|\Phi(t)\rangle|^2 = \langle\chi_i(t)|\chi_i(t)\rangle\,. \tag{1.34}$$

Let us again consider a particular case where only two electronic states are present (1.15). In Ref. [1], a measure of coherence $\mathcal{M}_\mathrm{coh}$ is defined as

$$\mathcal{M}_\mathrm{coh}(t) = \rho_{\mathrm{e},12}(t)\rho_{\mathrm{e},21}(t) + \rho_{\mathrm{e},21}(t)\rho_{\mathrm{e},12}(t) = 2|\langle\chi_1(t)|\chi_2(t)\rangle|^2. \tag{1.35}$$

By comparison with the electronic coherence (1.33), we see that

$$2\mathcal{M}_{\mathrm{coh}}(t) \geq C_{12}^2(t), \quad \forall t. \tag{1.36}$$

We can notice that using the Cauchy-Schwarz inequality on the last expression of (1.35), we obtain

$$\mathcal{M}_{\mathrm{coh}} \leq 2 \langle \chi_1(t)|\chi_1(t)\rangle \langle \chi_2(t)|\chi_2(t)\rangle = 2P_1(t)P_2(t). \tag{1.37}$$

Furthermore, the normalization of the total wave function (1.25),

$$P_1(t) + P_2(t) = 1, \tag{1.38}$$

provides us with the inequality

$$\mathcal{M}_{\mathrm{coh}}(t) \leq \frac{1}{2}. \tag{1.39}$$

The quantity $\mathcal{M}_{\mathrm{coh}}$ is maximal for equal populations,

$$P_1(t) = P_2(t) = \frac{1}{2}, \tag{1.40}$$

and the more the populations differ from being equal, the smaller is the upper estimate of $\mathcal{M}_{\mathrm{coh}}$. If one of the populations is zero, the upper estimate of $\mathcal{M}_{\mathrm{coh}}$ is zero, therefore, the value itself is zero (it is non-negative, as can be seen directly from (1.35)), resulting in the coherence being also zero. Essentially, if only one state is populated, we cannot speak of any coherence – there is nothing for the populated state to be coherent with. This gives us the first decoherence mechanism – "changes in electronic state populations due to non-adiabatic transitions" [1, p. 279]. We can see the schematic picture in Figure 1.1a.

If we write the (1.35) in the coordinate representation, we obtain

$$\mathcal{M}_{\mathrm{coh}}(t) = 2\left|\int \mathrm{d}\boldsymbol{R}\, \chi_1^*(\boldsymbol{R},t)\chi_2(\boldsymbol{R},t)\right|^2 \leq 2\left|\int \mathrm{d}\boldsymbol{R}\, |\chi_1(\boldsymbol{R},t)||\chi_2(\boldsymbol{R},t)|\right|^2. \tag{1.41}$$

We will call the integral in the last expression the *geometric overlap*. From this inequality, we can see the second decoherence mechanism – "relative motion of the nuclear wave packets on the different electronic states" [1, p. 279]. The schematic picture can be found in Figure 1.1b. If the geometric overlap of the states is zero, then the integrand $|\chi_1(\boldsymbol{R},t)||\chi_2(\boldsymbol{R},t)|$ must be zero for (almost) all configurations $\boldsymbol{R}$, i.e., there is at most one state "present" in any geometry, therefore, we again cannot speak of any coherence.

By introducing the absolute values into the integrand of (1.41), we neglected the relative $\boldsymbol{R}$- and t-dependent phase of the two states. Its effect is the third mechanism of decoherence – "an overall dephasing with time of the oscillations from the different wave packet components" [1, p. 279]. We will later see that the dephasing can be partially attributed to an effect similar to the second mechanism – loss of wave packet overlap in the momentum space. The schematic picture can be seen in Figure 1.1c.

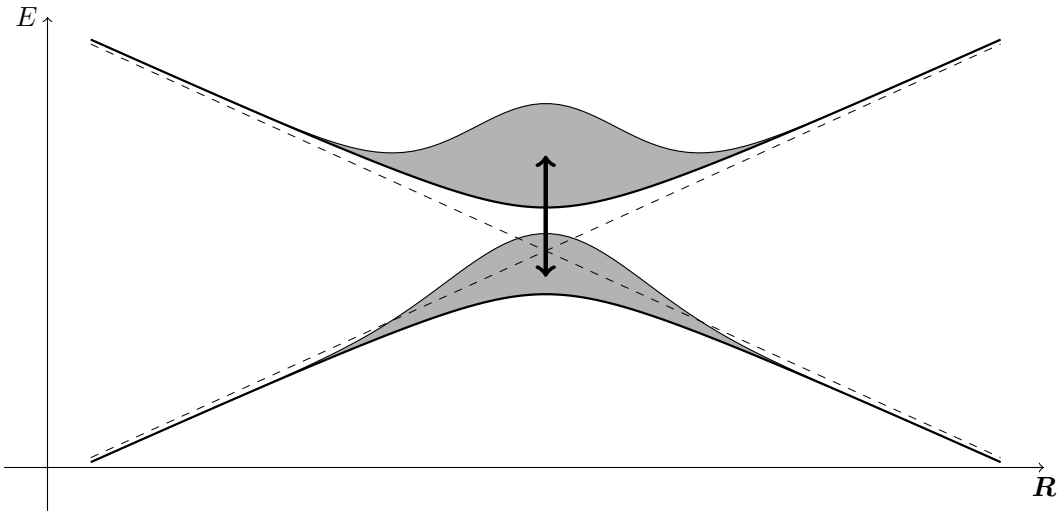

(a) Non-adiabatic transitions.

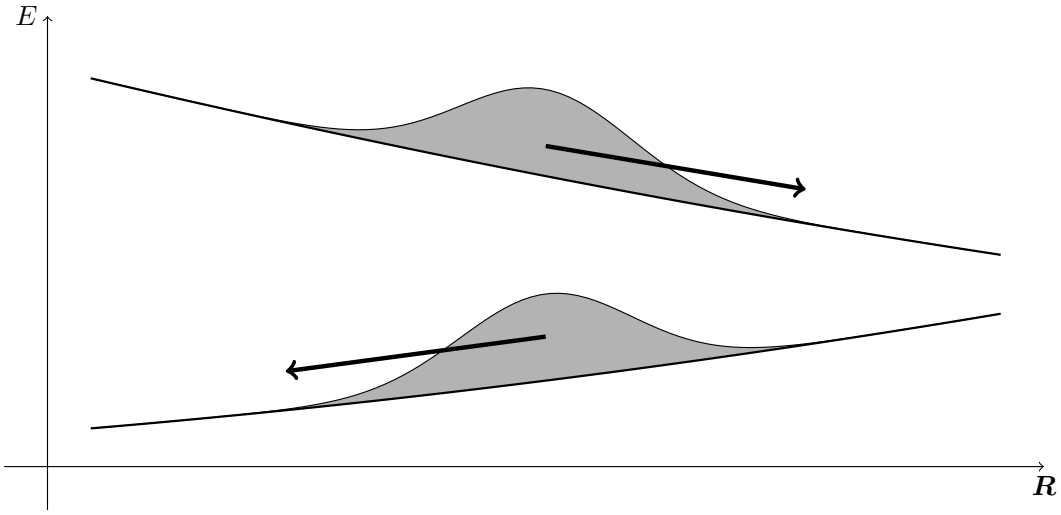

(b) Relative motion.

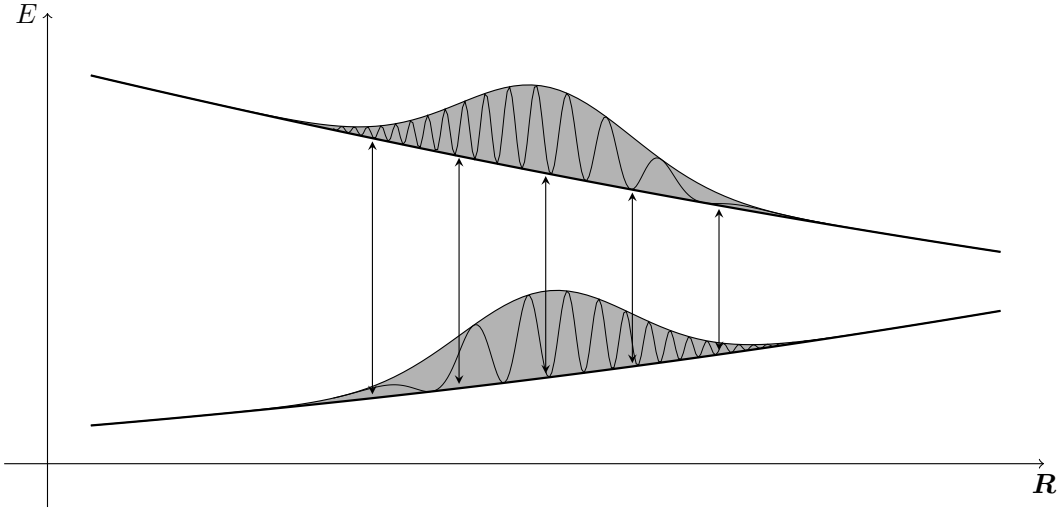

(c) Dephasing.

Figure 1.1: The three mechanisms of decoherence.

1.3.1 More on dephasing

The dephasing mechanism deserves more attention than what it was granted above. In Ref. [7], coherence and decoherence in a general context are discussed. The authors consider a system (the electrons, in our case) semiclassically interacting with a bath (the nuclei), predict decoherence and discuss the mechanisms causing it. They divide the system into two paths, only one of which is exposed to the bath, and then investigate the coherence between the two paths after the interaction. They approximate all the states with Gaussian wave packets and let them evolve using semiclassical perturbation theory equations, which allow for the separation of the motion of the wave packets and the phase they acquire during the interaction. The dephasing is then specified by the average of the phase factors over the bath states.

For illustration, let us present a schematic picture of the dephasing, somewhat similar to the one presented in [8]. Consider a one-dimensional nuclear coordinate space and two electronic states with their corresponding *potential energy curves* (PECs), $E_1(R)$ and $E_2(R)$, both populated with the same Gaussian nuclear wave packet,

$$\chi_{1,2}(R) = \frac{1}{\sqrt[4]{2\pi\sigma_{\mathrm{R}}^2}} \exp\left(-\frac{(R-R_0)^2}{4\sigma_{\mathrm{R}}^2}\right). \tag{1.42}$$

To isolate the dephasing mechanism, we fix these two wave packets in space by enforcing the stationary evolution given by the corresponding R-dependent energies $E_1(R)$, $E_2(R)$

$$\chi_{1,2}(R,t) = \mathrm{e}^{-iE_{1,2}(R)t}\chi_{1,2}(R). \tag{1.43}$$

We also expand the energies up to first order in the distance from the center of the wave packet R_0,

$$E_i(R) = E_i - F_i(R-R_0) + \mathcal{O}\Big((R-R_0)^2\Big), \tag{1.44}$$

$$\Delta E(R) \equiv \Delta E - \Delta F(R-R_0) + \mathcal{O}\Big((R-R_0)^2\Big). \tag{1.45}$$

Let us now evaluate the L^2 product of the two functions, which is the core of both the coherence $C_{12}(t)$ (1.14) and the $\mathcal{M}_{\mathrm{coh}}$ quantity (1.35),

$$\begin{aligned}\int \mathrm{d}R\, \chi_1^*(R,t)\chi_2(R,t) &= \frac{1}{\sqrt{2\pi\sigma_{\mathrm{R}}^2}} \int \mathrm{d}R\, \mathrm{e}^{-i(\Delta E-\Delta F(R-R_0))t} \mathrm{e}^{-\frac{(R-R_0)^2}{2\sigma_{\mathrm{R}}^2}} \\ &= \mathrm{e}^{-i(\Delta E+\Delta F R_0)t} \mathrm{e}^{iR_0\Delta F t} \mathrm{e}^{-\frac{(\Delta F t\sigma_{\mathrm{R}})^2}{2}} = \mathrm{e}^{-i\Delta E t} \mathrm{e}^{-\frac{\Delta F^2 t^2 \sigma_{\mathrm{R}}^2}{2}}.\end{aligned} \tag{1.46}$$

This simple picture predicts that dephasing causes $\approx \exp(-t^2)$ decoherence. If we wanted to suppress the effect that dephasing has on decoherence, we would have to make ΔF and σ_{R} as small as possible. This means making the PECs parallel and making the wave packet narrow. Parallel PECs also ensure that the wave packets move in the same way, therefore, this condition also suppresses the relative motion decoherence mechanism.

1.4 Measures of coherence

In this section, we summarize the already defined measures of coherence, add two more, and provide their mutual relations. Various groups studying the topic prefer different quantities to characterize coherence.

The first quantity is the above-defined (1.14) *electronic coherence* $C_{ij}(t)$. Let us repeat here the definition for convenience,

$$C_{ij}(t) \equiv \rho_{\mathrm{e},ij}(t) + \rho_{\mathrm{e},ji}(t). \tag{1.47}$$

It is given by the sum of two mutually symmetrically adjoint matrix elements of the electronic density operator, and as such, it is inherently basis-dependent. We use it to measure coherence manifested in time-oscillations of electronic observables, therefore, we represent the density operator in the basis of eigenstates of the electronic Hamiltonian. There is still the ambiguity of whether to use the diabatic or adiabatic basis that was discussed above. It is not widely used because if the state is coherent, it oscillates between -1 and 1, and as the state decoheres, the amplitude of the oscillations decreases, and the frequency may change. The preferred measures of coherence stay at a constant value for a coherent state and decrease to zero as the state decoheres. Nevertheless, C_{ij} is used, e.g., in [9].

A not yet mentioned measure is the *degree of coherence*, defined as

$$D_{ij}(t) \equiv \frac{|\rho_{\mathrm{e},ij}(t)|}{\sqrt{\rho_{\mathrm{e},ii}(t)\rho_{\mathrm{e},jj}(t)}} = \frac{|\rho_{\mathrm{e},ij}(t)|}{\sqrt{P_i(t)P_j(t)}}. \tag{1.48}$$

It is also basis-dependent and takes on values between 0 for an incoherent mixture and 1 for a coherent superposition. Thanks to the denominator, it is normalized to the populations of the two considered states which is useful especially when these change – in case of transitions between the electronic states. It is utilized, for example, in Refs. [10] or [11].

A very frequently used measure of coherence is the *purity* of the electronic reduced density operator

$$\mathrm{Tr}\,\hat{\rho}_{\mathrm{e}}^2(t). \tag{1.49}$$

Unlike the previous two quantities, purity is basis-independent. Its values range from 0 to 1. Although it is widely used, it is not, strictly speaking, a measure of coherence – it reaches its maximal value if the density operator represents a pure state. If this state is an eigenstate of the electronic Hamiltonian, we do not observe any coherent behaviour, both coherence and degree of coherence are 0, yet the purity is 1. On the other hand, one of its advantages is that it describes the whole electronic subsystem, unlike the two previous quantities that were defined for a combination of two states. Let us mention Refs. [12] and [4] that use purity to quantify coherence.

Lastly, let us repeat the definition of the $\mathcal{M}_{\mathrm{coh}}$ quantity

$$\mathcal{M}_{\mathrm{coh},ij}(t) = \rho_{\mathrm{e},ij}(t)\rho_{\mathrm{e},ji}(t) + \rho_{\mathrm{e},ji}(t)\rho_{\mathrm{e},ij}(t). \tag{1.50}$$

It is again defined for a combination of two electronic states and, therefore, it is basis-dependent. We already discussed its properties (1.37), (1.39), and relation

to coherence (1.36). It is also tightly connected with purity. Suppose we only have two electronic states. In that case, the purity reads

$$\operatorname{Tr}\hat{\rho}_{\mathrm{e}}^2(t) = \rho_{\mathrm{e},11}(t)\rho_{\mathrm{e},11}(t) + \rho_{\mathrm{e},12}(t)\rho_{\mathrm{e},21}(t) + \rho_{\mathrm{e},21}(t)\rho_{\mathrm{e},12}(t) + \rho_{\mathrm{e},22}(t)\rho_{\mathrm{e},22}(t). \tag{1.51}$$

The $\mathcal{M}_{\mathrm{coh},12}$, therefore, gathers the coherence-relevant terms of the purity, fixing its main drawback that we discussed above – $\mathcal{M}_{\mathrm{coh},12}$ is zero for a system in its eigenstate. Apart from being defined in Ref. [1], it is used, e.g., in [7] – the already mentioned article about coherence and decoherence in a general context.

1.5 Molecular photoionization

In order to observe coherent electron dynamics in molecules, we need to create a superposition of states of the molecule, and we need to create it as quickly as possible to make sure that the observed phenomena are related to the coherent dynamics and not the interaction with the superposition-creating system[2]. Photoionization by an ultrashort laser pulse is used to fulfill both of these conditions. By making the pulse as short as possible, we ensure that the interaction time is very short and also broaden the spectral bandwidth to the order of electronvolts, which is the typical difference of energies of the nearest excited states in molecules. We also assume that the process of ionization does not change the configuration of the molecule; this is called *vertical ionization*.

1.5.1 Schematic description of the monochromatic and dichromatic photoionization

We start by schematically describing the photoionization by monochromatic and dichromatic light. By schematically, we mean that we shall only concern ourselves with energy conservation. We will see that it is impossible to prepare a coherent superposition of states by monochromatic light.

Let us consider a neutral molecule in a ground electronic state $|E_0\rangle$ and a photon in a state $|\omega\rangle$. Denoting $|\chi\rangle$ the nuclear wave packet describing the ground vibrational state of the neutral molecule, the system before the photoionization is described by $|\chi\rangle\,|E_0\rangle\,|\omega\rangle$. Let the ionized molecule possess two bound electronic states $|E_i^*\rangle$, $i \in \{1,2\}$ such that they satisfy the inequality

$$E_0 + \omega - E_i^* \equiv \varepsilon_i > 0 \tag{1.52}$$

at the equilibrium geometry of the neutral molecule – the *Franck-Condon point*. Therefore, the following photoionization channels are open:

$$|\chi\rangle\,|E_0\rangle\,|\omega\rangle \to |\chi\rangle\,|E_i^*\rangle\,|\varepsilon_i\rangle\,.$$

The $|\varepsilon_i\rangle$ ($\varepsilon_i > 0$) denotes the photoelectron. We can see the schematic picture of the energy conservation in Figure 1.2a. The process, therefore, leads to a super-

[2]Furthermore, in Ref. [4], it is indicated that long laser pulses could lead to population of incoherent mixtures of electronic states, albeit in the case of photoexcitation.

position

$$|\psi\rangle = |\chi\rangle \sum_{i=1}^{2} \alpha_i |E_i^*\rangle |\varepsilon_i\rangle , \quad \sum_{i=1}^{2} |\alpha_i|^2 = 1. \tag{1.53}$$

The PESs associated with the cationic states $|E_i^*\rangle$ are in general different from each other and from the PES of the original state $|E_0\rangle$ which leads to the non-trivial coupled nuclear-electron dynamics described in previous sections.

We want to focus on the dynamics of the molecule, so the restriction on this subsystem is desirable. The formalism of the density operator is convenient for this purpose. Let us denote $\hat{\rho}$ the density operator corresponding to the superposition (1.53) and calculate the reduced density operator of the cationic subsystem $\hat{\rho_{\text{ion}}}$,

$$\begin{aligned} \hat{\rho} = |\chi\rangle \langle\chi| (\, &|\alpha_1|^2 |E_1^*\rangle |\varepsilon_1\rangle \langle E_1^*| \langle\varepsilon_1| + |\alpha_2|^2 |E_2^*\rangle |\varepsilon_2\rangle \langle E_2^*| \langle\varepsilon_2| \\ &+ \alpha_1 \alpha_2^* |E_1^*\rangle |\varepsilon_1\rangle \langle E_2^*| \langle\varepsilon_2| + \text{h.c. }) , \end{aligned} \tag{1.54}$$

$$\hat{\rho_{\text{ion}}} = \text{Tr}_{\text{photoelectron}} \hat{\rho} = |\chi\rangle \langle\chi| \left(|\alpha_1|^2 |E_1^*\rangle \langle E_1^*| + |\alpha_2|^2 |E_2^*\rangle \langle E_2^*| \right) . \tag{1.55}$$

We can express the density operator on the subspace of the molecular Hilbert space generated by the states $|\chi\rangle |E_1^*\rangle$ and $|\chi\rangle |E_2^*\rangle$ in the basis of these two states as the density matrix

$$\rho_{\text{ion}} = \begin{pmatrix} |\alpha_1|^2 & 0 \\ 0 & |\alpha_2|^2 \end{pmatrix}. \tag{1.56}$$

Note that the two states $|\chi\rangle |E_1^*\rangle$ and $|\chi\rangle |E_2^*\rangle$ are orthonormal thanks to the orthonormality of the electronic part, they are eigenstates of the electronic Hamiltonian, but they are not eigenstates of the molecular Hamiltonian. We see that the density matrix is diagonal, therefore, we can interpret it as a statistical mixture of the states $|\chi\rangle |E_1^*\rangle$ and $|\chi\rangle |E_2^*\rangle$ populated with probabilities $|\alpha_1|^2$ and $|\alpha_2|^2$, respectively. This does not lead to the coherent behaviour of the cation described in Section 1.1 that we would like to observe.

Now let us move to the dichromatic case. Consider two frequencies ω_1 and ω_2 such that both allow the transition to the two states of the cation via energy conservation (1.52). The corresponding photoelectron energies are generally different for the two photon frequencies, so the final superposition contains photoelectron states with four different energies. Let us assume that

$$\omega_1 - E_1^* = \omega_2 - E_2^*, \tag{1.57}$$

which effectively fixes two of the photoelectron energies to be equal. The schematic picture of the energy conservation with this condition is in Figure 1.2b. We thus populate the following state

$$|\psi\rangle = |\chi\rangle \left(\beta_{11} |E_1^*\rangle |\varepsilon_1\rangle + \beta_{12} |E_1^*\rangle |\varepsilon_2\rangle + \beta_{22} |E_2^*\rangle |\varepsilon_2\rangle + \beta_{23} |E_2^*\rangle |\varepsilon_3\rangle \right) . \tag{1.58}$$

The corresponding reduced cationic density operator is

$$\hat{\rho}_{\text{ion}} = \text{Tr}_{\text{photoelectron}} |\psi\rangle \langle\psi| = \tag{1.59}$$

$$= |\chi\rangle \langle\chi| (\, (|\beta_{11}|^2 + |\beta_{12}|^2) |E_1^*\rangle \langle E_1^*| + (|\beta_{23}|^2 + |\beta_{22}|^2) |E_2^*\rangle \langle E_2^*| \tag{1.60}$$

$$+ \beta_{12} \beta_{22}^* |E_1^*\rangle \langle E_2^*| + \text{h.c}) , \tag{1.61}$$

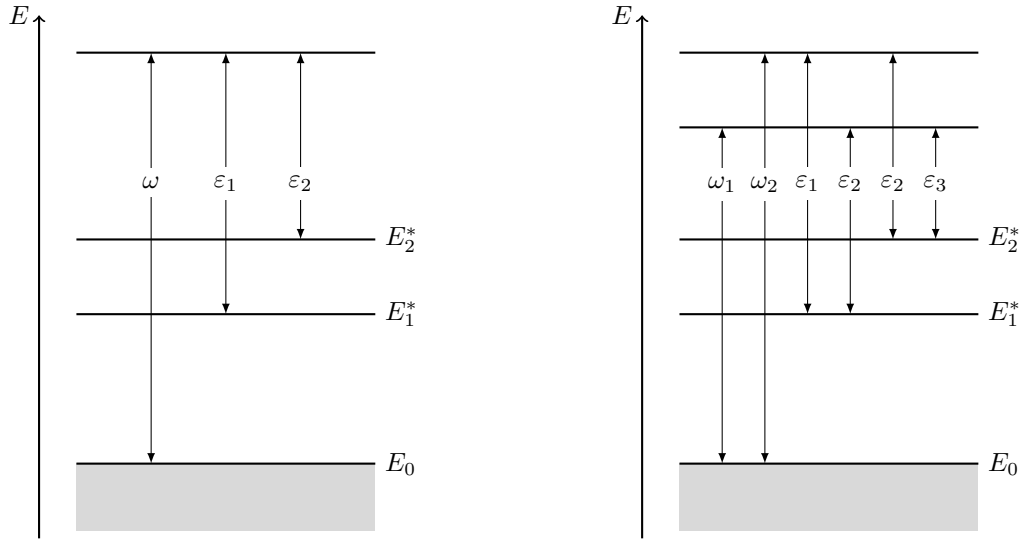

(a) Monochromatic photoionization. (b) Dichromatic photoionization.

Figure 1.2: The conservation of energy for the two described photoionization schemes.

or, on the same Hilbert subspace and in the same basis as in the monochromatic case above,

$$\rho_{\text{ion}} = \begin{pmatrix} |\beta_{11}|^2 + |\beta_{12}|^2 & \beta_{12}\beta_{22}^* \\ \beta_{12}^*\beta_{22} & |\beta_{23}|^2 + |\beta_{22}|^2 \end{pmatrix}. \tag{1.62}$$

In this case, we can see that in general, we have non-zero off-diagonal terms which can provide us with the desired coherent behaviour. Notice that these correspond to the terms of the populated state (1.58), which contain the photoelectron of the same energy ε_2. This observation becomes more evident when we set β_{11} and β_{23} equal to zero. In this case, the diagonal terms of the density matrix simplify. We can easily evaluate the purity of the cationic reduced density matrix

$$\operatorname{Tr} \rho_{\text{ion}}^2 = |\beta_{12}|^4 + 2|\beta_{12}|^2|\beta_{22}|^2 + |\beta_{22}|^4 = \left(|\beta_{12}|^2 + |\beta_{22}|^2\right)^2 = 1, \tag{1.63}$$

where the last equality follows from the normalization of the superposition (1.58). Therefore, we have a pure state containing, two electronic eigenstates; hence it has to be their fully coherent superposition if both β_{12} and β_{22} are non-zero.

We can relate the above discussion to the relationship between the entanglement of the photoelectron and the cation and the coherence within the cation. Looking at the populated state (1.58), we see that the two systems are the more entangled, the larger $|\beta_{11}|^2 + |\beta_{23}|^2$ is. If this value is equal to 1, the systems are fully entangled, and both β_{12} and β_{22} are equal to 0, which effectively reduces the state to the same form as in the case of monochromatic photoionization (1.53). The cation is in an incoherent statistical mixture of states. If, on the other hand, $|\beta_{11}|^2 + |\beta_{23}|^2 = 0$, i.e., the photoelectron and cation subsystems are not entangled, yielding a pure cationic state as we showed above, in (1.63).

1.5.2 Further aspects of photoionization

The electronic dynamics in molecules takes place on the attosecond timescale ($1\,\mathrm{as} = 10^{-18}\,\mathrm{s}$). Laser pulses with duration on a similar timescale are used to prepare states that lead to the coherent dynamics. Generation of sub-femtosecond ($1\,\mathrm{fs} = 10^{-15}\,\mathrm{s}$) laser pulses became possible only recently; 43 as laser pulse is the shortest one created to this day [13]. The time-energy uncertainty principle $\Delta E\,\Delta t \geq \hbar$, where in SI $\hbar \approx 10^{-34}\,\mathrm{J\,s}$, implies that any laser pulse with duration $\Delta t \lesssim 10^{-15}\,\mathrm{s}$ will have spectral bandwidth $\Delta E \gtrsim 10^{-19}\,\mathrm{J} \approx 1\,\mathrm{eV}$ which is the scale of the energy gaps between molecular electronic states.

By satisfying the condition on the duration of the laser pulse in order to not interfere with the observed electron dynamics (or with configuration changes), we simultaneously satisfy the other condition on populating a coherent superposition of a few electronic states. If we were to use even shorter laser pulses (once they are available), we would produce even broader bandwidths, resulting in a coherent population of many of cationic states, making it more challenging to interpret the results.

An interesting paper that studies the process of attosecond photoionization in more detail is [11]. They use the time-dependent configuration-interaction singles method to study the degree of coherence between ionic states in atomic xenon. They show that the coupling of the ionization channels enhances entanglement between the photoelectron and the cation, resulting in reduced cationic coherence. We already commented on the relationship between the entanglement of the cation and the photoelectron and the coherence within the cation. The reduction of the cationic coherence can be decreased by increasing the kinetic energy of the photoelectron, which can be regulated by controlling the mean photon energy.

This thesis focuses on the coupled electron-nuclear dynamics initiated by photoionization. In our model, we will populate directly the superposition or statistical mixture of electronic states of the cation, the evolution of which we want to study. We will not take the photoelectron into account. In Figure 1.3, we can see a schematic picture of the photoionization process. In practice, controlling the superposition/mixture produced by photoionization is challenging and requires cutting-edge laser technology to control the parameters of the laser pulses.

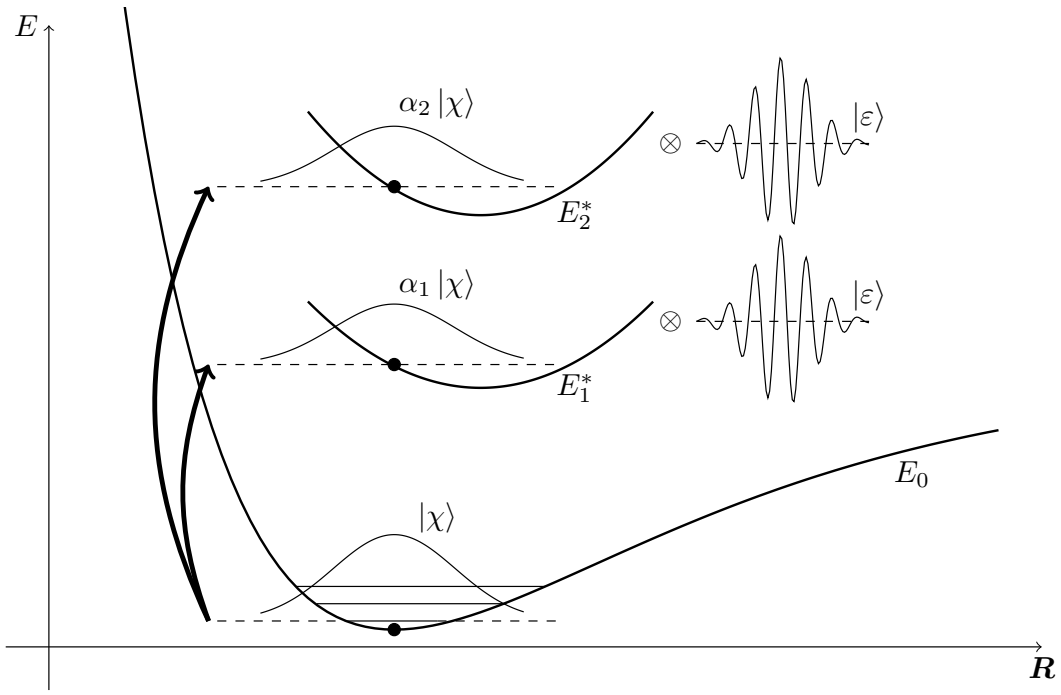

Figure 1.3: The schematic picture of photoionization from a ground state of the neutral molecule into a superposition of two states of the cation.

2. The model and numerical methods

In the previous chapter, we have introduced the topic of electronic decoherence. In this chapter, we shall formulate the model of molecular dynamics that we use to investigate the phenomenon. We also describe our approach to solving the coupled nuclear-electron dynamics within the model and mention the main utilized numerical methods.

2.1 The general approach

We consider a $(1+1)$D system described by the following Hamiltonian (in the coordinate representation)

$$\hat{H}_{\mathrm{tot}}(r,R) = -\frac{1}{2m}\frac{\partial^2}{\partial R^2} - \frac{1}{2}\frac{\partial^2}{\partial r^2} + V_{\mathrm{N-e}}(r,R) + V_{\mathrm{N}}(R), \tag{2.1}$$

where r is the electronic coordinate, R is the nuclear coordinate, $V_{\mathrm{N}}(R)$ is the potential of the nuclear subsystem, $V_{\mathrm{N-e}}(r,R)$ is the R-dependent potential of the electronic subsystem, and m is the *reduced mass* of the nuclear subsystem. The shape of the potentials is specified below. Note that the Hamiltonian terms resemble the terms of the molecular Hamiltonian (1.16), only the electron-electron interaction is missing. This is expected because, in our model, we only have one electron[1]. For convenience, let us also split the Hamiltonian into two parts,

$$\hat{T}_{\mathrm{N}}(R) = -\frac{1}{2m}\frac{\partial^2}{\partial R^2}, \tag{2.2}$$

$$\hat{H}_{\mathrm{e}}(r,R) = -\frac{1}{2}\frac{\partial^2}{\partial r^2} + V_{\mathrm{N-e}}(r,R) + V_{\mathrm{N}}(R), \tag{2.3}$$

the nuclear kinetic energy $\hat{T}_{\mathrm{N}}(R)$ and the electronic Hamiltonian $\hat{H}_{\mathrm{e}}(r,R)$.

Our approach is to solve the time-independent Schrödinger equation

$$\hat{H}_{\mathrm{tot}}(r,R)\Phi_j(r,R) = E_j\Phi_j(r,R), \tag{2.4}$$

express the initial state in terms of the eigenstates

$$\Phi_{\mathrm{init}}(r,R) = \sum_j \alpha_j \Phi_j(r,R), \tag{2.5}$$

and then determine the state of the system at an arbitrary time t as

$$\Phi(r,R,t) = \sum_j \alpha_j \mathrm{e}^{-iE_j t}\Phi_j(r,R). \tag{2.6}$$

Then, we can trivially construct the corresponding density matrix

$$\rho(r,R,r',R',t) = \Phi(r,R,t)\Phi^*(r',R',t). \tag{2.7}$$

[1] We could also consider the electronic part of the system to represent a hole, which would be more sensible in making analogies between our model and a cation, but it is otherwise irrelevant.

If we wish to compare the evolution of a coherent initial state with the evolution of an incoherent statistical mixture of initial states, we evolve each of them separately and then combine them into the density matrix

$$\rho_{\mathrm{mix}}(r, R, r', R', t) = \sum_i p_i \Phi_i(r, R, t) \Phi_i^*(r', R', t), \tag{2.8}$$

where p_i is the probability of the initial state being $\Phi_{\mathrm{init},i}(r, R)$. From the density matrix, we obtain the reduced electronic (or nuclear) density matrix by evaluating the partial trace over the nuclear (or electronic) subsystem. From the reduced density matrices, we can evaluate all the measures of coherence introduced in the first chapter and any other observable of the given subsystem.

2.2 The strictly diabatic representation

In Section 1.2, we discussed the adiabatic and the strictly diabatic representations in the context of solving the time-dependent Schrödinger equation corresponding to a general molecular Hamiltonian (1.16). The same ideas apply to the time-independent Schrödinger equation as well.

We want to continue without any approximations, and for this purpose, we find the strictly diabatic representation more convenient. When we introduce the basis and the potentials below, we will see that to obtain all the necessary matrix elements in this representation, we only need analytical derivatives and analytical and numerical quadratures. In the adiabatic representation, we would need analytical and numerical derivatives and analytical and numerical quadratures. The need for numerical derivatives would arise from the R-dependence of the electronic adiabatic eigenstates $\psi_i(r, R)$ and the nuclear kinetic energy operator $\hat{T}_{\mathrm{N}}$ acting on them.

Let us summarize the strictly diabatic representation approach in the present context. We start with the expansion

$$\Phi_i(r, R) = \sum_k \tilde{\psi}_k(r) \tilde{\chi}_{ik}(R), \tag{2.9}$$

where $\tilde{\psi}_k(r)$ is the solution of the electronic Schrödinger equation at a fixed value of nuclear coordinate $\widetilde{R}$ which may or may not be the equilibrium configuration,

$$\hat{H}_{\mathrm{e}}(r, \widetilde{R}) \tilde{\psi}_k(r) = \mathcal{E}_k \tilde{\psi}_k(r), \tag{2.10}$$

and $\tilde{\chi}_{ik}(R)$ are the solutions of the following equations

$$\hat{T}_{\mathrm{N}} \tilde{\chi}_{il}(R) + \sum_k \int \mathrm{d}r\, \tilde{\psi}_l^*(r) \hat{H}_{\mathrm{e}}(r, R) \tilde{\psi}_k(r) \tilde{\chi}_{ik}(R) = E_i \tilde{\chi}_{il}(R). \tag{2.11}$$

The expansion (2.9) is infinite and exact.

In the diabatic representation, the matrix

$$(\hat{H}_{\mathrm{e}}(R))_{kl} = \int \mathrm{d}r\, \tilde{\psi}_l^*(r) \hat{H}_{\mathrm{e}}(r, R) \tilde{\psi}_k(r) \tag{2.12}$$

is non-diagonal and is a local potential energy operator acting on the R-dependent functions, and the matrix

$$(\hat{T}_{\mathrm{N}}(R))_{kl} = \int \mathrm{d}r\, \tilde{\psi}_l^*(r) \hat{T}_{\mathrm{N}}(R) \tilde{\psi}_k(r) = \delta_{kl} \hat{T}_{\mathrm{N}}(R) \tag{2.13}$$

is a diagonal differential operator acting on the R-dependent functions. The diagonal elements $(H_{\mathrm{e}}(R))_{kk}$ are the diabatic PECs.

2.3 Finding the eigenstates in a specific basis

We choose N orthonormal functions

$$\{\mathrm{X}_\alpha(R)\}_{\alpha=1}^{N} \tag{2.14}$$

as the basis of the nuclear degree of freedom and, similarly, M orthonormal functions

$$\{\Psi_\beta(r)\}_{\beta=1}^{M} \tag{2.15}$$

as the basis of the electronic degree of freedom. These two sets of functions form the direct product basis of the 2D space of the total Hamiltonian

$$\{\mathrm{X}_\alpha(R)\Psi_\beta(r)\}_{\alpha=1,\beta=1}^{N,M}. \tag{2.16}$$

Let us call the above-defined bases the *primary nuclear basis*, the *primary electronic basis*, and the *primary (total) basis*, respectively.

At first, we will search for the solutions of the electronic time-independent Schrödinger equation as linear combinations of the primary electronic basis

$$\tilde{\psi}_k(r) = \sum_{\alpha=1}^{M} c_k^\alpha \Psi_\alpha(r). \tag{2.17}$$

Plugging this ansatz into (2.10) leads to the following equation

$$\sum_{\alpha=1}^{M} (H_\mathrm{e}|_{\widetilde{R}})_{\beta\alpha} c_k^\alpha = \mathcal{E}_k c_k^\beta, \tag{2.18}$$

$$\mathbb{H}_\mathrm{e}|_{\widetilde{R}} \boldsymbol{c}_k = \mathcal{E}_k \boldsymbol{c}_k, \tag{2.19}$$

where

$$(H_\mathrm{e}|_{\widetilde{R}})_{\beta\alpha} = \int \mathrm{d}r\, \Psi_\beta^*(r) \hat{H}_\mathrm{e}(r, \widetilde{R}) \Psi_\alpha(r). \tag{2.20}$$

Equation (2.19) is a standard matrix diagonalization problem. The matrix $\mathbb{H}_\mathrm{e}|_{\widetilde{R}}$ is Hermitian guaranteeing the existence of an orthonormal set $\{\boldsymbol{c}_k\}_{k=1}^{M}$. We, therefore, constructed an orthonormal set of functions $\{\tilde{\psi}_k(r)\}_{k=1}^{M}$. Moreover, if we choose the primary basis to be real, the matrix $\mathbb{H}_\mathrm{e}|_{\widetilde{R}}$ and its eigenvectors are also real, and we obtained an orthonormal set of real functions.

We continue with the evaluation of the $\tilde{\chi}_{ik}(R)$ functions by an analogous ansatz

$$\tilde{\chi}_{ik}(R) = \sum_{\alpha=1}^{N} d_{ik}^\alpha \, \mathrm{X}_\alpha(R). \tag{2.21}$$

Let us now introduce the multi-index notation $\gamma = (l, \beta)$, $\delta = (k, \alpha)$, with translation to a single index given by $\gamma = l + (\beta - 1)M$, analogously for δ. Plugging Eq. (2.21) into Eq. (2.11) yields

$$\sum_{\gamma=1}^{MN} (H_\mathrm{tot})_{\gamma\delta} d_i^\gamma = E_i d_i^\delta, \tag{2.22}$$

$$\mathbb{H}_\mathrm{tot} \boldsymbol{d}_i = E_i \boldsymbol{d}_i, \tag{2.23}$$

where

$$(H_{\mathrm{tot}})_{\gamma\delta} = \delta_{kl} \int \mathrm{d}R\, \mathrm{X}^*_\beta(R)\hat{T}_{\mathrm{N}}(R)\mathrm{X}_\alpha(R) + \iint \mathrm{d}R\, \mathrm{d}r\, \mathrm{X}^*_\beta(R)\tilde{\psi}^*_l(r)\hat{H}_{\mathrm{e}}(r,R)\mathrm{X}_\alpha(R)\tilde{\psi}_k(r). \tag{2.24}$$

Equation (2.23) is again a standard matrix diagonalization. Following the same arguments as above, we acquire a set of orthonormal eigenvectors $\{\boldsymbol{d}_i\}_{i=1}^{MN}$, which are real if both the original bases are real.

Gathering the results, we obtained the solutions of the time-independent Schrödinger equation (2.4) in the following form

$$\Phi_i(r,R) = \sum_{k=1}^{M}\sum_{\alpha=1}^{N} d^\alpha_{ik}\tilde{\psi}_k(r)\mathrm{X}_\alpha(R). \tag{2.25}$$

It is a set of orthonormal functions $\{\Phi_i(r,R)\}_{i=1}^{MN}$, which are real if the primary bases are chosen real. In other words, we introduced an *intermediate (total) basis* of the 2D space,

$$\{\mathrm{X}_\alpha(R)\tilde{\psi}_k(r)\}_{\alpha=1,k=1}^{N,M}. \tag{2.26}$$

Alternatively, we could search for the eigenstates of $\hat{H}_{\mathrm{tot}}$ using a direct ansatz in terms of the *primary (total) basis* (2.16). The reason for the intermediate step will be discussed later on.

2.4 The design of the potentials

We may want our model to represent a certain normal mode of molecular vibrations. In general, normal modes are found by expanding the molecular PES up to second order around the equilibrium geometry $\boldsymbol{R}_{\mathrm{eq}} \equiv \boldsymbol{0}$

$$\hat{H} = -\sum_i \frac{1}{2m_i}\frac{\partial^2}{\partial R_i^2} + \sum_{ij}\frac{1}{2}V_{ij}R_iR_j, \tag{2.27}$$

where we set the zero-order term to zero because it is a trivial energy offset. Then, introducing the mass-weighted coordinates

$$q_i = \sqrt{m_i}R_i, \tag{2.28}$$

$$\hat{H} = -\sum_i \frac{1}{2}\frac{\partial^2}{\partial q_i^2} + \sum_{ij}\frac{1}{2}B_{ij}q_iq_j, \tag{2.29}$$

and diagonalizing the expanded potential, the Hamiltonian reduces to a system of non-interacting harmonic oscillators and the eigenvectors $\boldsymbol{Q}$ define the sought-after normal modes,

$$\hat{H} = \sum_i \left(-\frac{1}{2}\frac{\partial^2}{\partial Q_i^2} + \frac{1}{2}\omega_i Q_i^2\right). \tag{2.30}$$

For details, see, e.g. [14], or [15]. Then, we may recast (2.1) into

$$\hat{H}_{\mathrm{tot}}(r,Q) = -\frac{1}{2}\frac{\partial^2}{\partial Q^2} - \frac{1}{2}\frac{\partial^2}{\partial r^2} + \tilde{V}_{\mathrm{N-e}}(r,Q) + \tilde{V}_{\mathrm{N}}(Q). \tag{2.31}$$

Now we specify the two potentials $V_{\mathrm{N}}(R)$ and $V_{\mathrm{N-e}}(r,R)$ in the model Hamiltonian (2.1). The above discussion of the normal modes justifies the model nuclear potential being a harmonic well

$$V_{\mathrm{N}}(R) = \frac{1}{2}m\omega_{\mathrm{N}}^2(R-R_0)^2 + E_{\mathrm{N}}, \tag{2.32}$$

where m is the nuclear reduced mass, ω is the angular frequency of the harmonic oscillator, R_0 is the equilibrium value of the nuclear coordinate, and E_{N} is an arbitrary energy offset.

The electronic potential is supposed to imitate two centers (nuclei) on which the electron density concentrates. To achieve this, we choose it to comprise two harmonic wells sewn together at the point of intersection, i.e.,

$$V_{\mathrm{L}}(r,R) = \frac{1}{2}\omega_{\mathrm{L}}^2(R)\left(r + \frac{r_0(R)}{2}\right)^2 + E_L(R), \tag{2.33}$$

$$V_{\mathrm{R}}(r,R) = \frac{1}{2}\omega_{\mathrm{R}}^2(R)\left(r - \frac{r_0(R)}{2}\right)^2 + E_R(R), \tag{2.34}$$

$$V_{\mathrm{N-e}}(r,R) = \begin{cases} V_{\mathrm{L}}(r,R), & r < \tilde{r}(R), \\ V_{\mathrm{R}}(r,R), & r \geq \tilde{r}(R), \end{cases} \tag{2.35}$$

where $V_{\mathrm{L}}(r,R)$ and $V_{\mathrm{R}}(r,R)$ are two harmonic potential wells analogous to the nuclear one and their parameters are in general R-dependent; $\tilde{r}(R)$ is the point of intersection of $V_{\mathrm{L}}(r,R)$ and $V_{\mathrm{R}}(r,R)$. The electronic potential, along with its parameters, is schematically depicted in Figure 2.1.

For completeness, we present the formulae for the point of intersection $\tilde{r}(R)$. If both the harmonic wells have the same width $\omega_{\mathrm{L}}(R) = \omega_{\mathrm{R}}(R) \equiv \omega(R)$, we get

$$\tilde{r}(R) = \frac{E_{\mathrm{R}}(R) - E_{\mathrm{L}}(R)}{\omega^2(R) r_0(R)}. \tag{2.36}$$

If, on the other hand, $\omega_{\mathrm{L}}(R) \neq \omega_{\mathrm{R}}(R)$, the condition of intersection leads to a quadratic equation with the discriminant

$$D(R) = 4r_0^2(R)\omega_{\mathrm{L}}^2(R)\omega_{\mathrm{R}}^2(R) - 8\left(\omega_{\mathrm{L}}^2(R) - \omega_{\mathrm{R}}^2(R)\right)\left(E_{\mathrm{L}}(R) - E_{\mathrm{R}}(R)\right). \tag{2.37}$$

If $D(R) < 0$, there is no point of intersection and one of the parabolas is "above" the other. This case is not of our interest. If $D(R) = 0$, we obtain one point of intersection

$$\tilde{r}(R) = -\frac{\omega_{\mathrm{L}}^2(R) + \omega_{\mathrm{R}}^2(R)}{2\left(\omega_{\mathrm{L}}^2(R) - \omega_{\mathrm{R}}^2(R)\right)} r_0(R). \tag{2.38}$$

Lastly, if $D(R) > 0$, there are two points of intersection,

$$\tilde{r}(R) = \frac{-\left(\omega_{\mathrm{L}}^2(R) + \omega_{\mathrm{R}}^2(R)\right) r_0(R) \pm \sqrt{D(R)}}{2\left(\omega_{\mathrm{L}}^2(R) - \omega_{\mathrm{R}}^2(R)\right)}. \tag{2.39}$$

The last remaining ambiguity of the model is the R-dependence of the parameters of the quadratic functions constituting the electronic potential $r_0(R)$, $\omega_{\mathrm{L}}(R)$,

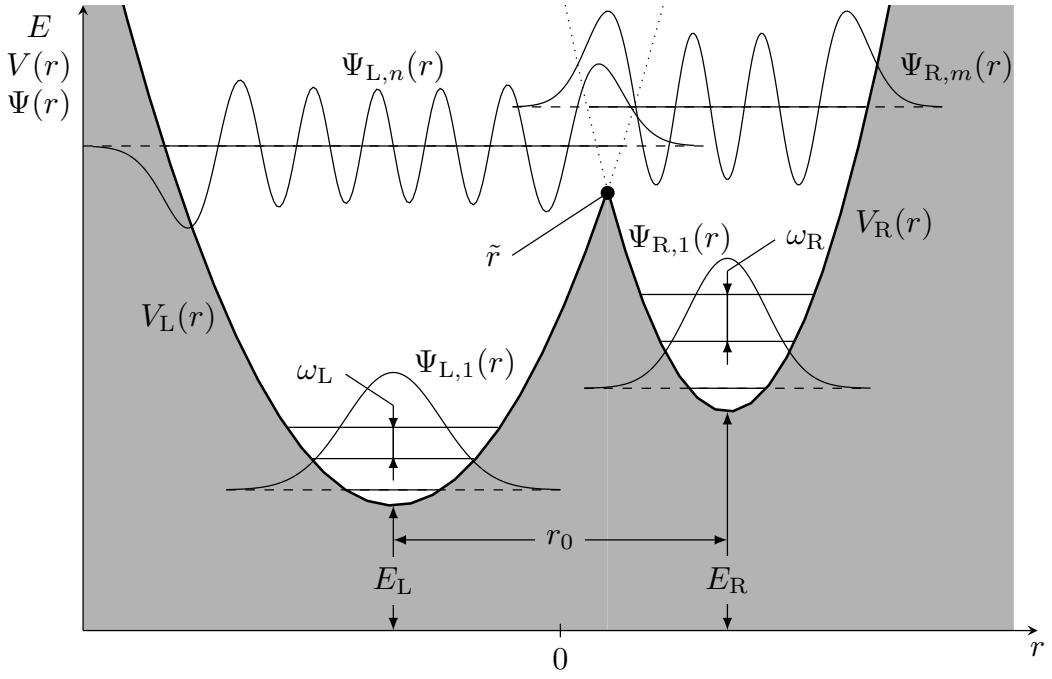

Figure 2.1: Schematic picture of the electronic potential $V_{\mathrm{e}}(r)$ consisting of the left $V_{\mathrm{L}}(r)$ and right $V_{\mathrm{R}}(r)$ part with the parameters r_0, ω_{L}, ω_{R}, E_{L}, and E_{R} (see text for details) and the point of intersection $\tilde{r}$ of the two parts. The picture also shows the first three energies of the harmonic potentials $V_{\mathrm{L}}(r)$ and $V_{\mathrm{R}}(r)$ and two of their eigenfunctions $\Psi_{\mathrm{L},i}(r)$, resp. $\Psi_{\mathrm{R},i}(r)$.

$\omega_{\mathrm{R}}(R)$, $E_{\mathrm{L}}(R)$, and $E_{\mathrm{R}}(R)$. We want these parameters to smoothly monotonously vary between two extremal values (which are both positive). The following functional form has been chosen

$$f(R) = \frac{f_{\max} - f_{\min}}{\pi} \arctan(a(R - R_0)) + \frac{f_{\max} + f_{\min}}{2}. \tag{2.40}$$

It is depicted in Figure 2.2, where we can see that in the vicinity of R_0, it is approximately a linear function with the slope given by the derivative

$$f'(R)|_{R_0} = \frac{f_{\max} - f_{\min}}{\pi}\, a. \tag{2.41}$$

2.5 The choice of the basis

Now that we have chosen the potentials, we can adjust our bases to them. More specifically, we adapt the nuclear basis (2.14) to the nuclear potential (2.32) and the electronic basis (2.15) to the electronic potential (2.35) with the nuclear coordinate fixed at a specific value $\widetilde{R}$.

Since we are dealing with harmonic potentials, we present the essential overview of information on their eigenfunctions. For a Hamiltonian

$$\hat{H} = \frac{\hat{p}^2}{2m} + \frac{1}{2} m\omega^2 \hat{x}^2, \tag{2.42}$$

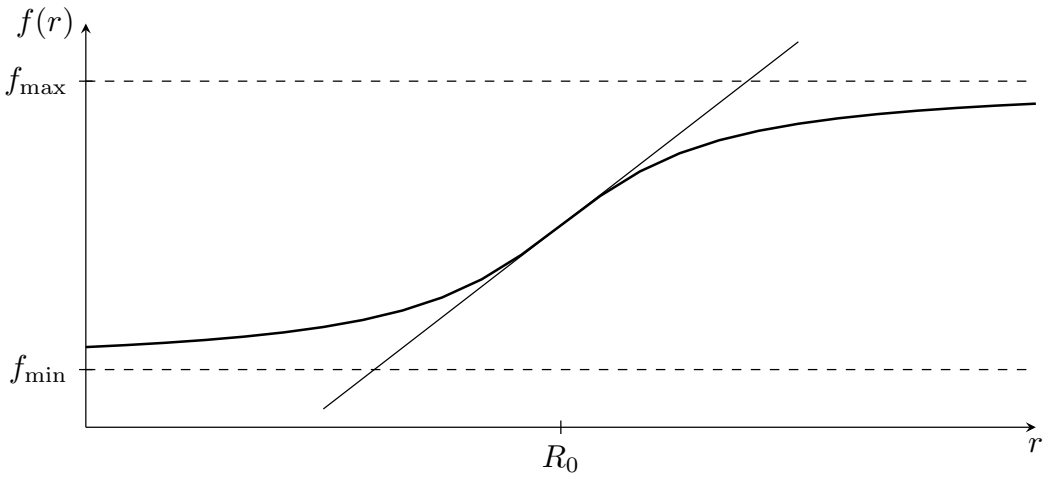

Figure 2.2: Schematic picture of the electronic adjusting function $f(R)$ with its asymptotes and a line approximating it at the point R_0.

the eigenenergies are

$$E_n = \omega\left(n + \frac{1}{2}\right), \quad n \in \mathbb{N}_0 \tag{2.43}$$

and the eigenfunctions

$$\psi_n(x) = \frac{1}{\sqrt{2^n n!}}\left(\frac{m\omega}{\pi}\right)^{\frac{1}{4}} \mathrm{e}^{-\frac{m\omega x^2}{2}} H_n(\sqrt{m\omega}\, x), \tag{2.44}$$

where $H_n(x)$ are the Hermite polynomials. The functions $\psi_n(x)$ are called the *Hermite functions*. Two useful identities for the Hermite functions can be derived from the properties of the Hermite polynomials, see, e.g., Ref. [16]

$$\sqrt{m\omega}\, x\, \psi_n(x) = \sqrt{\frac{n}{2}}\, \psi_{n-1}(x) + \sqrt{\frac{n+1}{2}}\, \psi_{n+1}(x), \tag{2.45}$$

$$\frac{1}{\sqrt{m\omega}}\, \psi_n'(x) = \sqrt{\frac{n}{2}}\, \psi_{n-1}(x) - \sqrt{\frac{n+1}{2}}\, \psi_{n+1}(x). \tag{2.46}$$

The first one is the recurrence relation we use to generate the functions, and the other is convenient for evaluating their derivatives. To start the recurrence, we also need the first two Hermite functions

$$\psi_0(x) = \left(\frac{m\omega}{\pi}\right)^{\frac{1}{4}} \mathrm{e}^{-\frac{m\omega x^2}{2}}, \tag{2.47}$$

$$\psi_1(x) = \frac{1}{\sqrt{2}}\left(\frac{m\omega}{\pi}\right)^{\frac{1}{4}} \mathrm{e}^{-\frac{m\omega x^2}{2}} 2\sqrt{m\omega}\, x. \tag{2.48}$$

Let us also mention the following inequality, see Ref. [17, p. 787]

$$|\psi_n(x)| \leq 0.816. \tag{2.49}$$

As the nuclear basis, the first N Hermite functions are used (with the appropriate parameters m, ω_{N}, and offset to R_0). Note that the index of the first

Hermite function is 0, whereas we started indexing the bases from 1. We choose the electronic basis to consist of two parts – the first M_L Hermite functions adjusted to $V_\mathrm{L}(r, \widetilde{R})$ and the first M_R Hermite functions adjusted to $V_\mathrm{R}(r, \widetilde{R})$; $M = M_\mathrm{L} + M_\mathrm{R}$ basis functions in total. The M_L and M_R are chosen so that we "cover" the energies of $V_\mathrm{L}(r, \widetilde{R})$ and $V_\mathrm{R}(r, \widetilde{R})$ from their ground value up to a common threshold. This yields

$$M_\mathrm{L} = \left[\frac{\omega_R M + \frac{1}{2}(\omega_\mathrm{L} - \omega_\mathrm{R}) + E_\mathrm{R} - E_\mathrm{L}}{\omega_\mathrm{L} + \omega_\mathrm{R}}\right], \tag{2.50}$$

$$M_\mathrm{R} = M - M_\mathrm{L}, \tag{2.51}$$

where the square brackets denote rounding to the nearest integer. Let us denote the two parts of the basis as follows

$$\{\Psi_\alpha(r)\}_{\alpha=1}^{M} = \{\Psi_{\mathrm{L},\alpha}(r)\}_{\alpha=1}^{M_L} \cup \{\Psi_{\mathrm{R},\alpha}(r)\}_{\alpha=1}^{M_R}. \tag{2.52}$$

2.5.1 Symmetric orthogonalization

There is a slight problem with the above choice of the electronic basis – it is not precisely orthonormal. The reason can be seen in Figure 2.1 – the functions of the two parts of the basis overlap. We need to generate a set of M mutually orthogonal eigenfunctions of the electronic Hamiltonian from a set of M linearly independent functions.

The appropriate method is called *Löwdin's symmetric orthogonalization* (see the original paper [18]). Using the ansatz (2.17), we obtain the following variations of (2.18) and (2.19)

$$\sum_{\alpha=1}^{M} (H_\mathrm{e}|_{\widetilde{R}})_{\beta\alpha}\, c_k^\alpha = \mathcal{E}_k \sum_{\alpha=1}^{M} S_{\beta\alpha}\, c_k^\alpha, \tag{2.53}$$

$$\mathbb{H}_\mathrm{e}\, \boldsymbol{c}_k = \mathcal{E}_k \mathbb{S}\, \boldsymbol{c}_k, \tag{2.54}$$

where $(H_\mathrm{e}|_{\widetilde{R}})_{\beta\alpha}$ is given by (2.20), and

$$S_{\beta\alpha} = \int \mathrm{d}r\, \Psi_\beta^*(r)\Psi_\alpha(r). \tag{2.55}$$

The overlap matrix $\mathbb{S}$ is Hermitian, therefore, its eigenvectors form an orthonormal basis, and we can write

$$\mathbb{S} = \mathbb{U}\Lambda\mathbb{U}^\mathrm{T}, \tag{2.56}$$

where $\Lambda = \mathrm{diag}(\lambda_1, \ldots, \lambda_M)$, λ_i are the eigenvalues, and $\mathbb{U}$ contains the eigenvectors as its columns. Using this decomposition, we can calculate any function of the overlap matrix, namely, $1/\sqrt{\mathbb{S}}$ will be of use. We multiply (2.54) by it from the left and obtain

$$\frac{1}{\sqrt{\mathbb{S}}}\, \mathbb{H}_\mathrm{e} \frac{1}{\sqrt{\mathbb{S}}} \sqrt{\mathbb{S}}\, \boldsymbol{c}_k = \mathcal{E}_k \sqrt{\mathbb{S}}\, \boldsymbol{c}_k \iff \widetilde{\mathbb{H}}_\mathrm{e}\, \tilde{\boldsymbol{c}}_k = \mathcal{E}_k \tilde{\boldsymbol{c}}_k. \tag{2.57}$$

The last equation is the standard eigenvalue problem of a Hermitian matrix $\widetilde{\mathbb{H}}_\mathrm{e}$. From its eigenvectors, we can evaluate the solutions of (2.54) as

$$\boldsymbol{c}_k = \frac{1}{\sqrt{\mathbb{S}}}\, \tilde{\boldsymbol{c}}_k. \tag{2.58}$$

Another problem arising when we make the primary electronic basis large is that it becomes numerically linearly dependent. This manifests in the eigenvalues of $\mathbb{S}$ being close to zero, which complicates the evaluation of $1/\sqrt{\mathbb{S}}$. This problem can be treated by using the *pseudoinverse* approach. First, we order the eigenvalues of $\mathbb{S}$ from largest to smallest (they are non-negative), reordering the columns of $\mathbb{U}$ correspondingly. We can write out the decomposition (2.56) as

$$\mathbb{S} = \begin{pmatrix} \boldsymbol{u}_1 & \cdots & \boldsymbol{u}_{\widetilde{M}} & \cdots & \boldsymbol{u}_M \end{pmatrix} \begin{pmatrix} \lambda_1 & & & & \\ & \ddots & & 0 & \\ & & \lambda_{\widetilde{M}} & & \\ & 0 & & \ddots & \\ & & & & \lambda_M \end{pmatrix} \begin{pmatrix} \boldsymbol{u}_1^{\mathrm{T}} \\ \vdots \\ \boldsymbol{u}_{\widetilde{M}}^{\mathrm{T}} \\ \vdots \\ \boldsymbol{u}_M^{\mathrm{T}} \end{pmatrix} \tag{2.59}$$

where all λ_i, $i > \widetilde{M}$ are lower than our chosen deletion threshold $\lambda_{\mathrm{cutoff}}$. By discarding these eigenvalues, we effectively obtain

$$\mathbb{S} = \widetilde{\mathbb{U}}\widetilde{\Lambda}\widetilde{\mathbb{U}}^{\mathrm{T}} \tag{2.60}$$

$$\mathbb{S} = \begin{pmatrix} \boldsymbol{u}_1 & \cdots & \boldsymbol{u}_{\widetilde{M}} \end{pmatrix} \begin{pmatrix} \lambda_1 & & 0 \\ & \ddots & \\ 0 & & \lambda_{\widetilde{M}} \end{pmatrix} \begin{pmatrix} \boldsymbol{u}_1^{\mathrm{T}} \\ \vdots \\ \boldsymbol{u}_{\widetilde{M}}^{\mathrm{T}} \end{pmatrix}. \tag{2.61}$$

Using the above, we can multiply (2.54) by $\left(\widetilde{\Lambda}\right)^{-1/2}\mathbb{U}^{\mathrm{T}}$ from the right and rewrite it as

$$\frac{1}{\sqrt{\widetilde{\Lambda}}}\,\widetilde{\mathbb{U}}^{\mathrm{T}}\mathbb{H}_{\mathrm{e}}\,\widetilde{\mathbb{U}}\frac{1}{\sqrt{\widetilde{\Lambda}}}\sqrt{\widetilde{\Lambda}}\,\widetilde{\mathbb{U}}^{\mathrm{T}}\boldsymbol{c}_k = \mathcal{E}_k\sqrt{\widetilde{\Lambda}}\,\widetilde{\mathbb{U}}^{\mathrm{T}}\boldsymbol{c}_k \iff \widetilde{\mathbb{H}}_{\mathrm{e}}\,\tilde{\boldsymbol{c}}_k = \mathcal{E}_k\tilde{\boldsymbol{c}}_k. \tag{2.62}$$

The last equation is again a standard eigenvalue problem. Solving it yields $\widetilde{M}$ vectors from whom we can obtain $\widetilde{M}$ solutions of (2.54) as

$$\boldsymbol{c}_k = \mathbb{U}\frac{1}{\sqrt{\widetilde{\Lambda}}}\,\tilde{\boldsymbol{c}}_k. \tag{2.63}$$

We have reduced the electronic basis by $M - \widetilde{M}$ and the 2D basis (2.26) by $(M - \widetilde{M})N$ functions. This reduction is the primary reason for the above-discussed intermediate step in the process of finding the eigenstates of the total Hamiltonian $\hat{H}_{\mathrm{tot}}$.

2.6 The matrix elements

Now, let us summarize the matrix elements that we have to evaluate. We start with the electronic equation (2.53). We need the overlap matrix $\mathbb{S}$ defined by (2.55) and the matrix of the Hamiltonian (2.20), which can be separated into three terms,

$$\begin{aligned}(H_{\mathrm{e}}|_{\widetilde{R}})_{\alpha\beta} &= \int \mathrm{d}r\, \Psi_\alpha^*(r)\left(-\frac{1}{2}\frac{\partial^2}{\partial r^2} + V_{\mathrm{N-e}}(r,\widetilde{R}) + V_{\mathrm{N}}(\widetilde{R})\right)\Psi_\beta(r) \\ &= (T_{\mathrm{e}})_{\alpha\beta} + (V_{\mathrm{N-e}}|_{\widetilde{R}})_{\alpha\beta} + V_{\mathrm{N}}(\widetilde{R})S_{\alpha\beta}.\end{aligned} \tag{2.64}$$

The required matrix elements are gathered in Tab. 2.1, along with the methods of their evaluation. The analytical formula for the elements of $\mathbb{T}_{\mathrm{e}}$ satisfying $A = B$ (see Tab. 2.1) is

$$(T_{\mathrm{e}})_{\mathrm{AA},\alpha\beta} = \frac{\omega_A}{4}\left((2\alpha+1)\delta_{\alpha\beta} - \sqrt{\alpha(\alpha-1)}\,\delta_{\alpha-1,\beta+1} + \sqrt{(\alpha+1)(\alpha+2)}\,\delta_{\alpha+1,\beta-1}\right). \tag{2.65}$$

For the second step, we need the matrix elements of the total Hamiltonian defined by (2.24). We can separate it into four terms

$$\begin{aligned}(H_{\mathrm{tot}})_{\gamma\delta} &= \delta_{kl}\int \mathrm{d}R\, \mathrm{X}^*_\alpha(R)\hat{T}_{\mathrm{N}}(R)\mathrm{X}_\beta(R) \\ &\quad + \iint \mathrm{d}R\,\mathrm{d}r\, \mathrm{X}^*_\alpha(R)\tilde{\psi}^*_k(r)\left(-\frac{1}{2}\frac{\partial^2}{\partial r^2} + V_{\mathrm{N-e}}(r,R) + V_{\mathrm{N}}(R)\right)\mathrm{X}_\beta(R)\tilde{\psi}_l(r) \\ &= \delta_{kl}(T_{\mathrm{N}})_{\alpha\beta} + \delta_{kl}(V_{\mathrm{N}})_{\alpha\beta} + \delta_{\alpha\beta}(\widetilde{T}_{\mathrm{e}})_{kl} + (V_{\mathrm{N-e}})_{\alpha k,\beta l},\end{aligned} \tag{2.66}$$

where we used the orthonormality of $\{\mathrm{X}_\alpha(R)\}$ and $\{\tilde{\psi}_k(r)\}$. The first two terms can be combined into the purely nuclear Hamiltonian

$$(H_{\mathrm{N}})_{\alpha\beta} \equiv (T_{\mathrm{N}})_{\alpha\beta} + (V_{\mathrm{N}})_{\alpha\beta}. \tag{2.67}$$

The required matrix elements are gathered in Tab. 2.2, along with the methods of their evaluation. The analytical formula for elements of $\mathbb{H}_{\mathrm{N}}$ is

$$\delta_{\alpha\beta}\left(\omega_{\mathrm{N}}\left(\alpha+\frac{1}{2}\right) + E_{\mathrm{N}}\right). \tag{2.68}$$

Table 2.1: The required matrix elements of the electronic operators in the primary electronic basis and their evaluation methods. We denote $A, B \in \{\mathrm{L},\mathrm{R}\}$.

matrix	definition of the matrix element	evaluation
$\mathbb{S}$	$\int \mathrm{d}r\, \Psi^*_{A,\alpha}(r)\Psi_{B,\beta}(r)$	$\begin{cases} = \delta_{\alpha\beta}, & A = B, \\ \text{numerically}, & A \neq B, \end{cases}$
$\mathbb{T}_{\mathrm{e}}$	$-\frac{1}{2}\int \mathrm{d}r\, \Psi^*_{A,\alpha}(r)\frac{\partial^2}{\partial r^2}\Psi_{B,\beta}(r)$	$\begin{cases} \text{analytically, Eq. (2.65)}, & A = B, \\ \text{numerically}, & A \neq B, \end{cases}$
$\mathbb{V}_{\mathrm{N-e}}$	$\int \mathrm{d}r\, \Psi^*_{A,\alpha}(r)V_{\mathrm{N-e}}(r,\widetilde{R})\Psi_{B,\beta}(r)$	numerically

2.7 Numerical quadrature

The numerical quadrature of our choice is the *composite Gauss-Legendre formula*. Let us briefly summarize its definition (see Ref. [16]). For a given set of *quadrature nodes* $\{x_k\}_{k=1}^n$, we define a general *interpolatory quadrature rule* as

$$\int_a^b f(x)w(x)\,\mathrm{d}x = \sum_{k=1}^n w_k f(x_k) + E_n(f), \tag{2.69}$$

Table 2.2: The required matrix elements of the total Hamiltonian terms in the intermediate total basis and their evaluation methods.

matrix	definition of the matrix element	evaluation
$\mathbb{H}_{\mathrm{N}}$	$\int \mathrm{d}R\, \mathrm{X}^*_\alpha(R) \left(\hat{T}_{\mathrm{N}}(R) + V_{\mathrm{N}}(R)\right) \mathrm{X}_\beta(R)$	analytically, Eq. (2.68)
$\widetilde{\mathbb{T}}_{\mathrm{e}}$	$-\frac{1}{2}\int \mathrm{d}r\, \tilde{\psi}^*_k \frac{\partial^2}{\partial r^2} \tilde{\psi}_l(r)$	transformation of $\mathbb{T}_{\mathrm{e}}$
$\mathbb{V}_{\mathrm{N-e}}$	$\iint \mathrm{d}R\, \mathrm{d}r\, \mathrm{X}^*_\alpha(R) \tilde{\psi}^*_k(r) V_{\mathrm{N-e}}(r,R) \mathrm{X}_\beta(R) \tilde{\psi}_l(r)$	numerically

with the condition $E_n(f) = 0$ for all f polynomials of degree $\leq 2n-1$. We call $w(x)$ the *weight function*, $\{w_k\}_{k=1}^n$ the *quadrature weights* and $E_n(f)$ the *error term*.

Consider a set of monic polynomials $\{p_n\}$ orthogonal with respect to a positive weight function $w(x)$ on an interval (a,b). The set $\{x_k\}_{k=1}^n$ of roots of such a polynomial p_n defines the so-called *Gauss quadrature* whose weights and error term are as follows

$$w_k = \int_a^b \frac{p_n(x)}{(x-x_k)p_n'(x_k)} w(x)\, \mathrm{d}x\,, \tag{2.70}$$

$$E_n(f) = \gamma_n \frac{f^{(2n)}(\xi)}{(2n)!}, \tag{2.71}$$

where $\xi \in (a,b)$ (specific but unknown), and

$$\gamma_n = \int_a^b p_n^2(x) w(x)\, \mathrm{d}x\,. \tag{2.72}$$

The quadrature is exact for polynomials of degree $\leq 2n-1$. In general, we can estimate the error by

$$E_n(f) \leq \gamma_n \frac{\max\limits_{(a,b)} |f^{(2n)}|}{(2n)!}. \tag{2.73}$$

Specifically, if $\{p_n\}$ are the monic Legendre polynomials, we have the *Gauss-Legendre quadrature*

$$(a,b) = (-1,1), \quad w(x) = 1, \quad \gamma_n = \frac{2^{2n+1}}{2n+1} \frac{(n!)^4}{((2n)!)^2}. \tag{2.74}$$

The quadrature can be naturally rescaled to a general interval (a,b)

$$x_k \to \tilde{x}_k = \frac{(b-a)x_k + a + b}{2}, \tag{2.75}$$

$$w_k \to \tilde{w}_k = w_k \frac{b-a}{2}. \tag{2.76}$$

$$\gamma_n \to \tilde{\gamma}_n = \gamma_n \left(\frac{b-a}{2}\right)^{2n+1}. \tag{2.77}$$

The final step is the *composite Gauss-Legendre quadrature*, see, e.g., Ref. [19]. If we split the quadrature interval (a, b) into N subintervals of equal length $h = (b - a)/N$, we obtain the error estimate

$$E_{N,n}(f) \leq \frac{\gamma_n}{N^{2n}} \left(\frac{b-a}{2}\right)^{2n+1} \frac{\max\limits_{(a,b)} |f^{(2n)}|}{(2n)!}. \tag{2.78}$$

If we require integral precision $E_{N,n}(f) \leq \varepsilon_{\text{prec}}$, then for a composite n-point Gauss-Legendre quadrature, we need at least

$$N = \left\lceil \left(\frac{\gamma_n}{\varepsilon_{\text{prec}}} \left(\frac{b-a}{2}\right)^{(2n+1)} \frac{\max\limits_{(a,b)} |f^{(2n)}|}{(2n)!} \right)^{\frac{1}{2n}} \right\rceil \tag{2.79}$$

subintervals.

We adjust our quadrature rules to the integrals constituting the $\mathbb{S}$, $\mathbb{T}_{\text{e}}$, and $\mathbb{V}_{\text{e}}$ matrices (see Tab. 2.1) for the r-quadrature and the $\mathbb{H}_{\text{N}}$ matrix for the R-quadrature (see Tab. 2.2). The determination of the quadrature parameters comes in two steps. First, we determine the quadrature interval (a, b) so that the integral over $(-\infty, a) \cup (b, \infty)$ is $\leq \varepsilon_{\text{prec}}$. Second, we use (2.79) to minimize the total number $N \times n$ of quadrature nodes for optimal efficiency. In both steps, we use the fact that the integrands are products of Hermite functions, their derivatives, and polynomials, and apply the recurrence relation (2.45), the identity for the derivative (2.46), and the inequality (2.49) for Hermite functions. We use the same quadrature rules for the integrals comprising the $\mathbb{V}_{\text{N}-\text{e}}$ matrix (see Tab. 2.2). Adapting the quadrature to these integrals would be more complicated because of the non-polynomial R-dependence of $V_{\text{N}-\text{e}}(r, R)$.

3. Results and discussion

We shall now discuss the results provided by the model described in Chapter 1. We will start with the uncoupled electron and nuclear dynamics that preserves electronic coherence. Then we will discuss three fundamental cases of coupled dynamics characterized by one of the parameters of the coupling potential $V_{\mathrm{N-e}}(r, R)$ being R-dependent. Finally, we apply our model to describe the three normal modes of vibration of the H_2O molecule.

Before we begin with the discussion, let us make a few notes. In Table 1.1, we defined the electronic density $\rho(r, t)$ in four different ways. In what follows, we will use the definition

$$\rho(r, t) = \int \mathrm{d}R\, \rho(r, R, r, R, t), \tag{3.1}$$

where $\rho(r, R, r', R', t)$ is the full time-dependent density matrix in coordinate representation. Speaking in terms of Table 1.1, this corresponds to either Case A or Case C, depending on the used separation of the system (diabatic or adiabatic, respectively). Let us similarly define the nuclear density

$$\rho(R, t) = \int \mathrm{d}r\, \rho(r, R, r, R, t). \tag{3.2}$$

In this chapter, we shall, for brevity, denote the strictly diabatic states in coordinate representation as $\psi_i(r)$, instead of $\psi_i(r; R_0)$ or $\tilde{\psi}_i(r)$.

3.1 Uncoupled electron and nuclear dynamics

First, let us investigate the uncoupled electron and nuclear dynamics, i.e., the case where the coupling potential $V_{\mathrm{N-e}}(r, R)$ (see Section 2.4) is R-independent, reducing to $V_{\mathrm{N-e}}(r)$. In this case, electrons (r) and nuclei (R) are separate non-interacting systems.

We start with a model defined in Figure 3.1. In panel (a), we see the electronic potential $V_{\mathrm{N-e}}(r)$ and its two lowest eigenstates. Note that the adiabatic and (strictly) diabatic states are identical in the uncoupled case. In panel (b), we can see the PECs of this model (again, the adiabatic ones are identical to the diabatic ones). The adiabatic PECs correspond simply to the nuclear potential $V_{\mathrm{N}}(R)$ offset by the eigenvalues E_i of the electronic potential $V_{\mathrm{N-e}}(r)$,

$$\mathrm{PEC}_i(R) = V_{\mathrm{N}}(R) + E_i. \tag{3.3}$$

In Figure 3.2, we can see the evolution of the four measures of electronic coherence defined in Section 1.4 for four different initial conditions (see the caption for details). We see that the evolution, in fact, does not depend on the geometry at which we populate the nuclear wave packet. If we populate a coherent superposition, the electronic subsystem stays coherent. All the measures indicate full coherence; the purity $\mathrm{Tr}\,\rho_{\mathrm{e}}^2$ is 1, as well as the degree of coherence D_{12}. The *coherence* C_{12} oscillates between -1 and 1, and $\mathcal{M}_{\mathrm{coh},12}$ is $1/2$, indicating that both states are equally populated (see equation (1.37) and the following text). If we populate a statistical mixture, it stays a mixture. The degree of coherence,

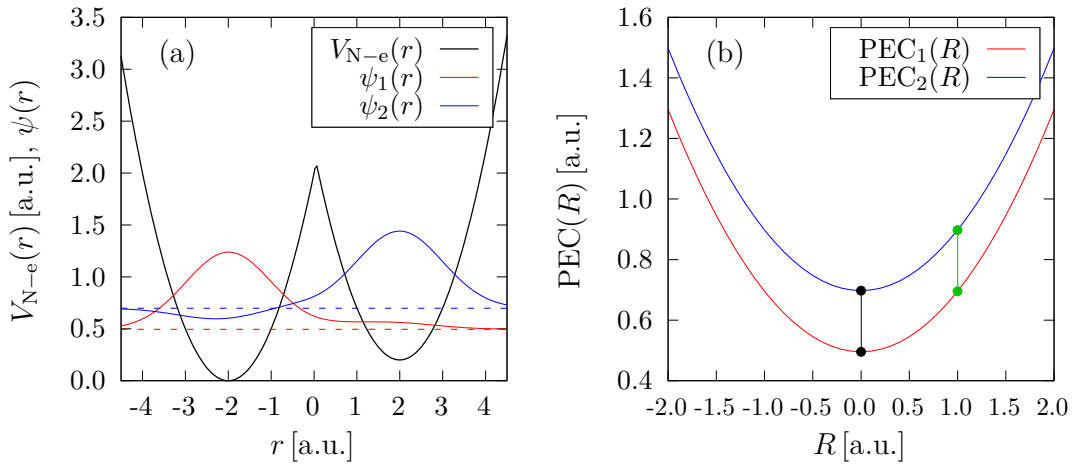

Figure 3.1: (a) A potential $V_{N-e}(r)$ with the following parameters (all given in atomic units): $R_0 = 0$, $\omega_N = 0.02$, $m = 1000$, $E_N = 0$, $r_0 = 4$, $\omega_L = 1$, $\omega_R = 1$, $E_L = 0$, and $E_R = 0.2$. The eigenstates (solid lines) with the two lowest energies (dashed lines): $E_1 \approx 0.49554$ a.u., $E_2 \approx 0.69764$ a.u., are also shown. (b) Two lowest PECs in this model. Black and green dots indicate the states whose evolution we study.

$C_{1,2}$, and $\mathcal{M}_{\text{coh},12}$ are 0, and the purity is 1/2, which agrees with the fact that for a completely incoherent mixture of N states, the purity is

$$\operatorname{Tr} \hat{\rho}^2 = \frac{1}{N}. \tag{3.4}$$

Figure 3.3 shows the evolution of the electronic $\rho(r,t)$ and the nuclear $\rho(R,t)$ densities. Again, we can observe the uncoupled behaviour. The evolution of the nuclear density is given solely by the populated nuclear wave packet. It does not depend on whether we populate a coherent superposition or an incoherent mixture of electronic states. Analogously, the evolution of the electronic density is given by the coherent character of the initial state. We also see that if we populate the nuclear wave packet in the nuclear potential $V_N(R)$ equilibrium, it stays there and does not move. In contrast, if we populate it at a different position, it oscillates around the equilibrium. As the nuclear wave packet moves in a harmonic potential, the period of oscillations is given by

$$T_{\text{nuc}} = \frac{2\pi}{\omega_N} = 100\pi \text{ a.u.} \approx 314 \text{ a.u.}, \tag{3.5}$$

which agrees with the corresponding panels of Figure 3.3. The evolution of the electronic density is trivial for a statistical mixture. For a coherent superposition, we observe oscillations with a period of $T_{\text{ele}} \approx 32$ a.u., which corresponds to the angular frequency

$$\omega = \frac{2\pi}{T_{\text{ele}}} \approx 0.2 \text{ a.u.} \tag{3.6}$$

The oscillations are caused by the energy gap between the two states, $E_2 - E_1 \approx 0.2$ a.u.

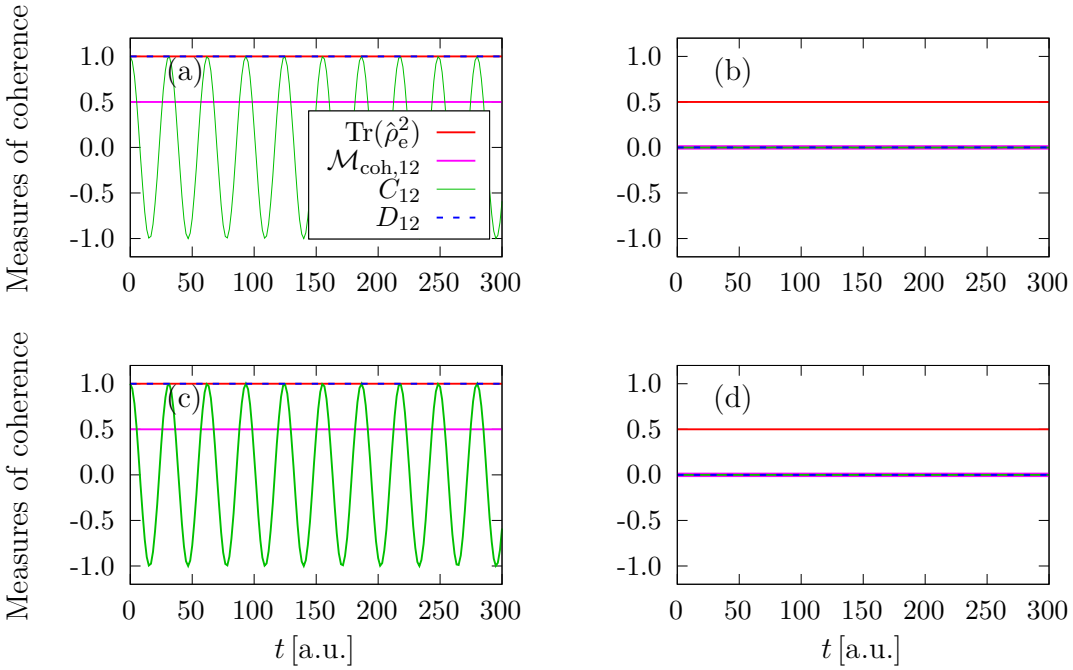

Figure 3.2: Evolution of measures of coherence in a model defined in Figure 3.1 and with different initial conditions. (a) A coherent superposition at equilibrium geometry $R = 0$ a.u. (b) An incoherent mixture at equilibrium geometry $R = 0$ a.u. (c) A coherent superposition at $R = 1$ a.u. (d) An incoherent mixture at $R = 1$ a.u. Note that in panels (a) and (c), the data lines corresponding to $\mathrm{Tr}(\rho_\mathrm{e}^2)$ and D_{12} are identical, and in panels (b) and (c), the data lines corresponding to $\mathcal{M}_{\mathrm{coh},12}$, C_{12}, and D_{12} are identical. Both superpositions and mixtures are populated with equal weights $1/\sqrt{2}$ and $1/2$, respectively.

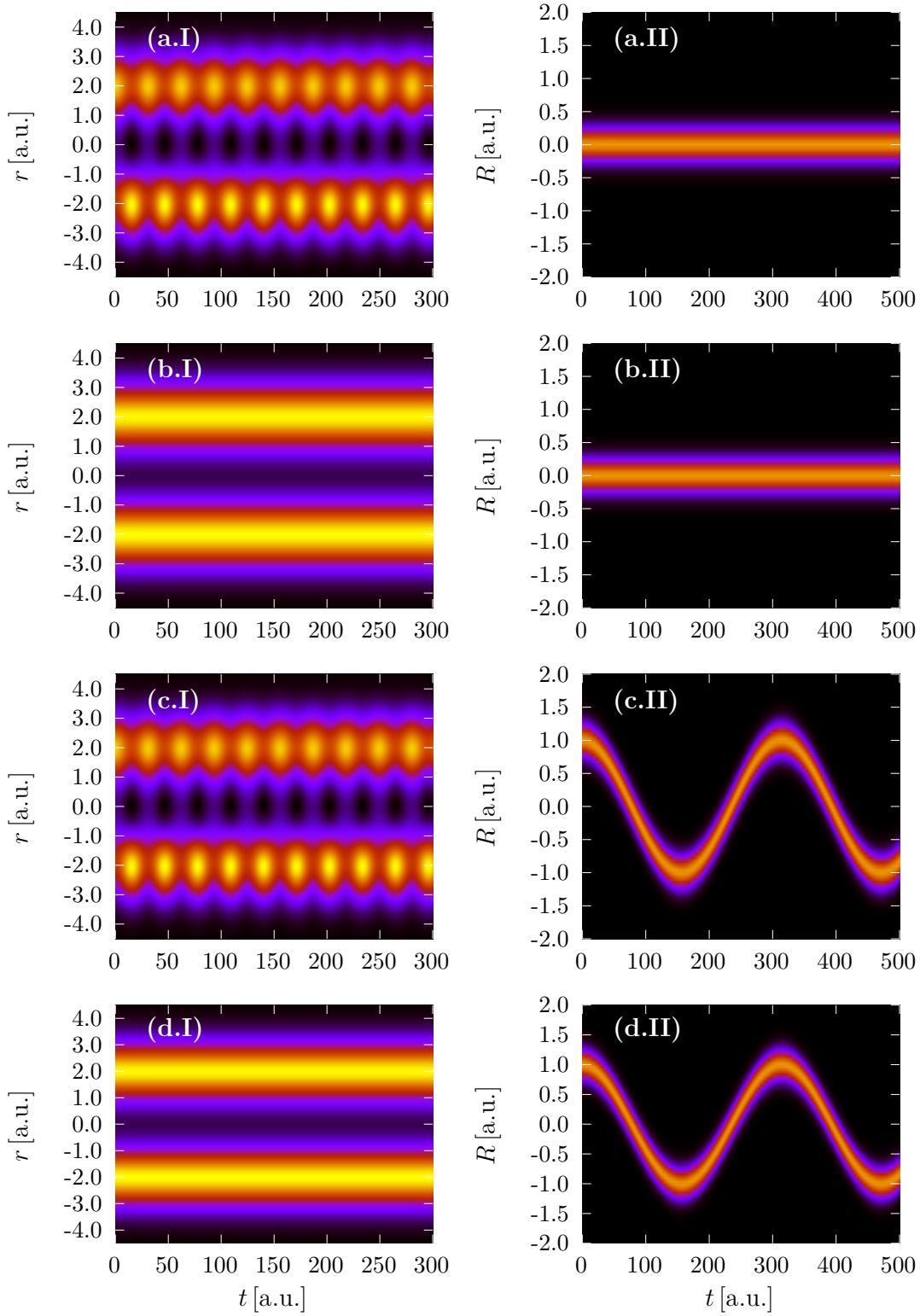

Figure 3.3: Evolution of electronic $\rho(r,t)$ (left panels) and nuclear $\rho(R,t)$ (right panels) densities in the model defined in Figure 3.1 and with different initial conditions. (a) Coherent superposition at equilibrium geometry $R = 0\,\text{a.u.}$ (b) Incoherent mixture at equilibrium geometry $R = 0\,\text{a.u.}$ (c) Coherent superposition at $R = 1\,\text{a.u.}$ (d) Incoherent mixture at $R = 1\,\text{a.u.}$ Both superpositions and mixtures are populated with equal weights $1/\sqrt{2}$ and $1/2$, respectively.

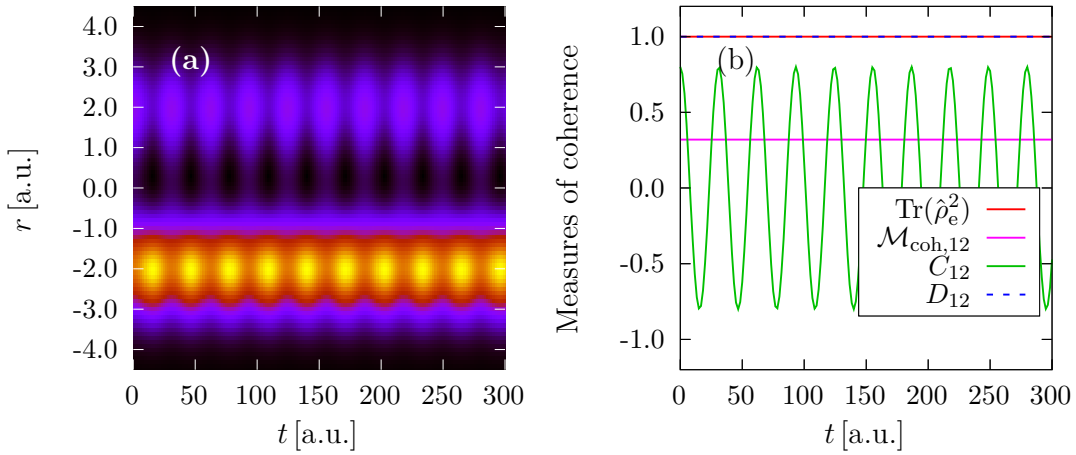

Figure 3.4: Evolution of (a) electronic density $\rho(r,t)$ and (b) measures of coherence in the model defined in Figure 3.1. A superposition of the two lowest electronic states was populated, with the coefficients $\sqrt{2/3}$ and $1/\sqrt{3}$. A Gaussian wave packet at $R = 1$ a.u. was populated in the nuclear degree of freedom. Note that in panel (b), the data lines corresponding to $\mathrm{Tr}(\rho_e^2)$ and D_{12} are identical.

In Figure 3.4, we see the evolution of electronic density and measures of coherence for an initial condition given by a coherent superposition with non-equal populations. We observe oscillations in the electronic density, which is more concentrated in the more populated state. The purity and the degree of coherence are 1, supporting their convenience for the cases where population dynamics occurs. The C_{12} and $\mathcal{M}_{\mathrm{coh},12}$ measures are slightly suppressed. In general, we would need additional information to decipher whether the superposition is not fully coherent or the populations are not equal.

Lastly, in Figure 3.5, we can see a coherent model with different parameters. The corresponding evolution of the coherence measures and the two densities for a coherent superposition is shown in respective panels. The measures of coherence indicate coherent behaviour, but we do not observe any oscillations in the electronic density. Recall the discussion from the end of Section 1.1, where we have shown that for the coherent behaviour to be visible in electronic density oscillations, the transition density (1.12) must be non-zero. In this case, the corresponding transition density matrix element reduces to

$$T_{12}(r) = \psi_1^*(r)\psi_2(r). \tag{3.7}$$

Looking at panel (a) of Figure 3.5, we see that the two states do not overlap, which explains the non-oscillatory behaviour of electronic density. One can also check that in the previous case (Figure 3.1), the overlap was non-trivial.

In Figure 3.5, we populated the nuclear degree of freedom with a ground state of a harmonic potential with $\omega = 0.01$ a.u. This state is wider than an eigenstate of the nuclear potential V_{N} within the model. In the evolution of nuclear density in panel (d), we can see that it periodically narrows and broadens with the same period with which it moves in the coordinate space. This is a well-known feature of Gaussian wave packet dynamics in the harmonic potential.

This concludes the discussion of the non-coupled electron and nuclear dynamics, which preserves the coherence of the initial condition. We have not seen

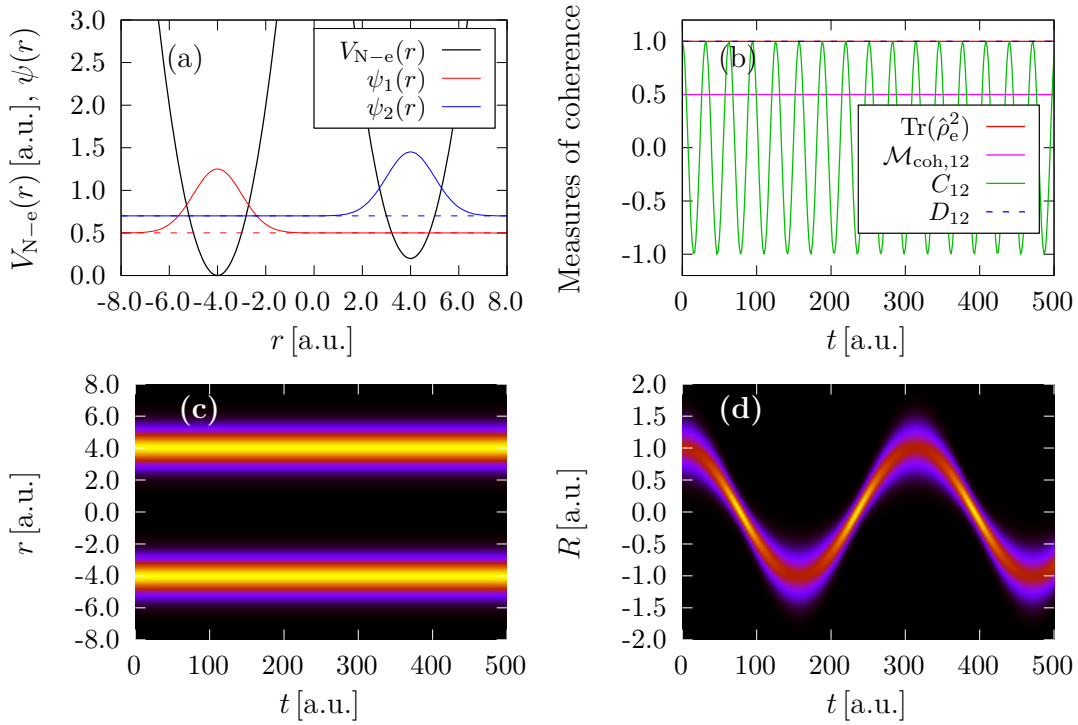

Figure 3.5: (a) A potential $V_{N-e}(r)$ with parameters (in atomic units): $r_0 = 8$, $\omega_L = 1$, $\omega_R = 1$, $E_L = 0$ and $E_R = 0.2$. It is accompanied by the nuclear potential $V_N(R)$ with parameters (in atomic units): $R_0 = 0$, $\omega_N = 0.02$, $m = 1000$, and $E_N = 0$. We populate a coherent superposition of the two shown electronic eigenstates, both with coefficients $1/\sqrt{2}$. (b) Evolution of the measures of coherence. Note that the data lines corresponding to $\mathrm{Tr}(\rho_e^2)$ and D_{12} are identical. (c) Evolution of the electronic density $\rho(r,t)$. (d) Evolution of the nuclear density $\rho(R,t)$. We populated a nuclear wave packet centered at $R = 1$ a.u.

anything surprising; the system behaves as expected. The primary purpose was to lay the ground for comparisons with the coupled cases.

3.2 Basic modes of electron-nuclear coupling

Let us now discuss three basic modes of electron-nuclear coupling that our model can describe. They are given by the R-dependence of individual parameters of $V_{\mathrm{N-e}}(r, R)$ (see Section 2.4), while all the others are fixed. The three distinct options are $r_0(R)$, $E_{\mathrm{L}}(R)$, and $\omega_{\mathrm{L}}(R)$.

3.2.1 Variable distance of the wells

At first, we investigate the case where the distance of the minima of the two potential wells comprising $V_{\mathrm{N-e}}(r, R)$ is R-dependent, and the other parameters are fixed. The specific values are given in the caption of Figure 3.6. Panel (a) shows the adiabatic PECs of this model, and panels (b)–(d) show R-cuts of the potential and the respective adiabatic states. We see a strong R-dependence of the adiabatic states, not only in their r-position but also in their shape – they become delocalized if the two harmonic wells are close to each other (see panel (b)). The adiabatic states are significantly different from the strictly diabatic ones. This indicates that we should use the adiabatic separation (see Section 1.2) of the density matrix for the evaluation of the measures of electronic coherence. Essentially, when the nuclear wave packet is at a particular geometry $\widetilde{R}$, we want the electronic states whose coherence we measure to be the ones that are the solutions of the electronic problem at that geometry $\widetilde{R}$. This is because we expect the electrons to "follow" the movement of the nuclei. If we used the diabatic separation, we would see an emergence of significant population of the strictly diabatic states that we have not initially populated. This would complicate using the coherence measures C_{ij}, D_{ij}, and $\mathcal{M}_{\mathrm{cal},12}$, because they are defined for a combination of two electronic states. In conclusion, using the diabatic representation would complicate the interpretation of the results.

Since we have chosen the adiabatic separation, we will also use the electronic adiabatic states for the initial superposition. If we used the diabatic ones, more adiabatic states would be present in the expression in terms of the adiabatically separated total wave function. The ratio of the "unwanted" admixture would be the larger, the wider the initial nuclear wave packet. Moreover, we could even observe that the initial state does not have full electronic coherence because we would use a different definition of the electronic subsystem than the one in which the initial electronic state is coherent.

To summarize, we use the adiabatic representation and populate a superposition of adiabatic electronic states. More specifically, we populate an equal-weight superposition of the two lowest adiabatic states and the nuclear wave packet corresponding to the ground state of the nuclear potential $V_{\mathrm{N}}(R)$ offset to $R_0 = 1\,\mathrm{a.u.}$

Panels (e) and (f) of Figure 3.6 show the evolution of the coherence measures. Panel (e) shows that the electronic subsystem is coherent until $t \approx 140\,\mathrm{a.u.}$, then the coherence decreases, and from $t \approx 300\,\mathrm{a.u.}$, it is an incoherent mixture. We also observe a significant partial coherence revival in $2000\,\mathrm{a.u.} \lesssim t \lesssim 2400\,\mathrm{a.u.}$

Panels (g) and (h) of Figure 3.6 show the electronic and nuclear density evolution, respectively. Initially, there are no visible oscillations of the electronic density due to negligible overlap of the two states caused by relatively large inter-well distance r_0. The overlap increases as the wells move closer, and we start to observe the oscillations. At the same time, decoherence ensues and dampens the oscillations. We see that the nuclear wave packet splits into two parts. Intuitively, we can attribute them to the two adiabatic PECs. Their turning points are $R_1 \approx 1.8\,\text{a.u.}$ and $R_2 \approx 0.9\,\text{a.u.}$, which agrees with the classical turning points of the adiabatic PECs in panel (a).

Recall the end of Section 1.3.1, where we discussed that to suppress decoherence, we need to make the PECs parallel at the point where the nuclear wave packet is populated. The PECs are parallel for $R \gtrsim 0\,\text{a.u.}$ This is the reason for the decoherence not to set in immediately. Looking at the evolution of nuclear density, we see that the wave packet reaches $R \approx 0\,\text{a.u.}$ at $t \approx 150\,\text{a.u.}$, which is when decoherence begins.

We now want to determine which decoherence mechanisms play a role in this case. Before we do that, we remind the quantities that will allow us to do so. We will investigate the population dynamics by the populations $P_i(t)$ themselves and use the degree of coherence $D_{ij}(t)$ to measure the decoherence caused by the other mechanisms. Let us properly define the *geometric overlap* mentioned in Section 1.3,

$$O_{R,ij}(t) = \int \mathrm{d}R\, |\chi_i^*(R,t)||\chi_j(R,t)|. \tag{3.8}$$

An analogous quantity, the *momentum overlap*, can be defined as

$$O_{P,ij}(t) = \int \mathrm{d}P\, |\widehat{\chi}_i^*(P,t)||\widehat{\chi}_j(P,t)|, \tag{3.9}$$

where $\widehat{\chi}_i(P,t)$ is the *Fourier transform* of $\chi_i(R,t)$ and P denotes the momentum. For better comparison with the degree of coherence, we also introduce the *normalized geometric (momentum) overlap* as

$$\widetilde{O}_{R,ij}(t) = \frac{O_{R,ij}(t)}{\sqrt{P_i(t)P_j(t)}}, \tag{3.10}$$

$$\widetilde{O}_{P,ij}(t) = \frac{O_{P,ij}(t)}{\sqrt{P_i(t)P_j(t)}}. \tag{3.11}$$

Using the definition (1.48) of the degree of coherence D_{ij}, yields the following inequalities

$$D_{ij} \leq \widetilde{O}_{R,ij}, \quad D_{ij} \leq \widetilde{O}_{P,ij}, \quad D_{ij} \leq \sqrt{\widetilde{O}_{R,ij}\widetilde{O}_{P,ij}} \equiv \widetilde{O}_{RP,ij}. \tag{3.12}$$

The momentum overlap and its product with geometric overlap were used to characterize the decoherence mechanisms in [10].

In Figure 3.7, we can see the evolution of the quantities essential for understanding the decoherence mechanisms. Panel (a) shows the population dynamics. We can see that the populations stay at approximately 1/2. There are fluctuations of relative magnitude of 3 % in three moments of the displayed time interval. These fluctuations do not disappear upon increasing the size of the used

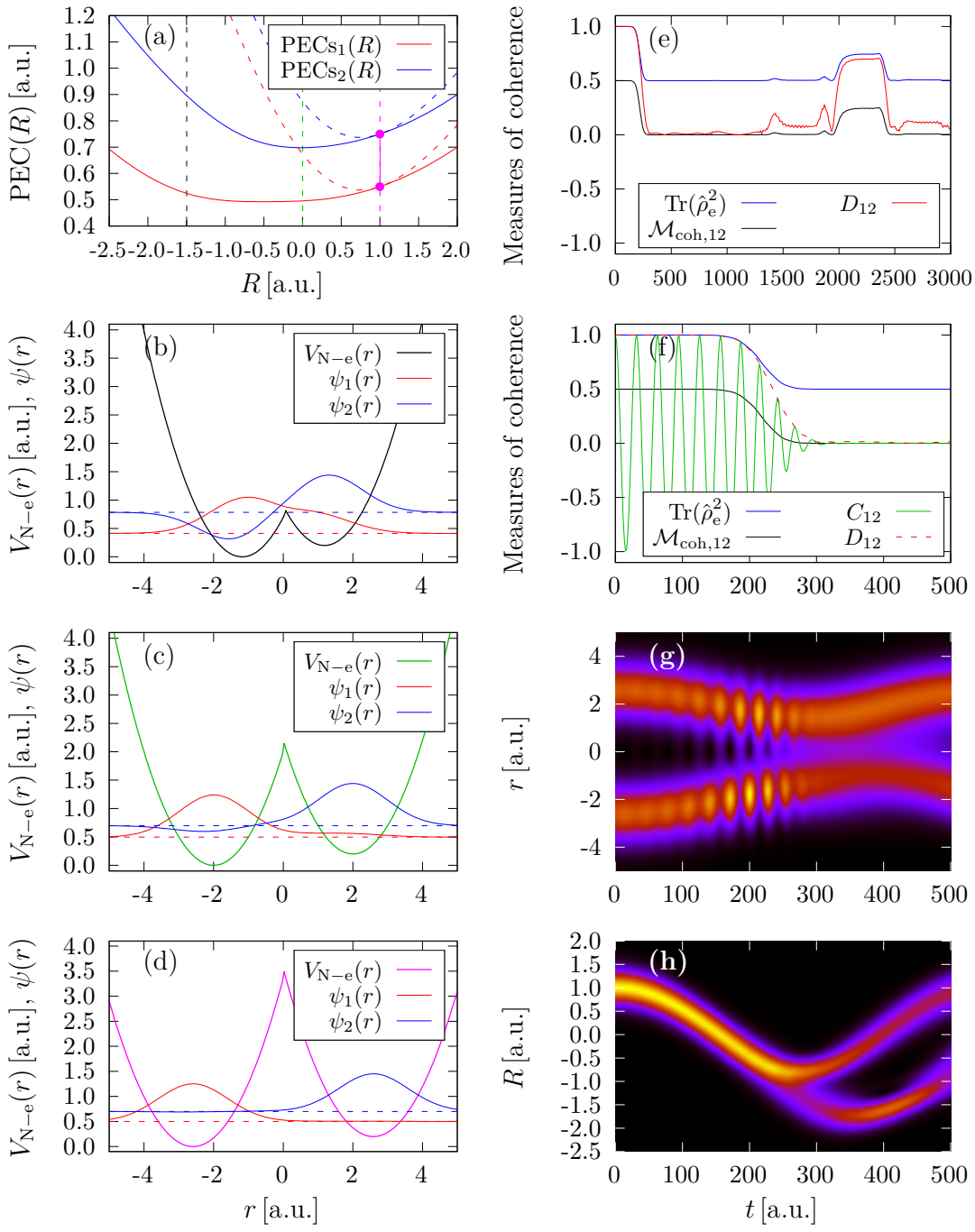

Figure 3.6: (a) Adiabatic (solid lines) and diabatic (dashed lines) PECs for a model with the following parameters (in atomic units): $R_0 = 0$, $\omega_{\mathrm{N}} = 0.01$, $m = 1000$, $E_{\mathrm{N}} = 0$, $r_{0,\mathrm{min}} = 0$, $r_{0,\mathrm{max}} = 8$, $a_{r_0} = 0.5$, $\omega_{\mathrm{L}} = 1$, $\omega_{\mathrm{R}} = 1$, $E_{\mathrm{L}} = 0$, and $E_{\mathrm{R}} = 0.2$. The magenta dots indicate the initial state whose evolution we study, coherent superposition (of adiabatic states) with equal weights $1/\sqrt{2}$ was populated. Adiabatic separation is used. The black, green, and magenta dashed lines indicate the geometries at which the R-cuts of the electronic adiabatic states in panels (b), (c), and (d), respectively, are calculated. (e) Evolution of the measures of coherence of the system. Coherence C_{12} is not shown because its oscillations are too fast for this range on the time axis. (f) A closer look at the initial decoherence. (g) Evolution of the electronic density $\rho(r, t)$. (h) Evolution of the nuclear density $\rho(R, t)$.

basis, therefore, they are not a numerical artifact but rather indicate a weak non-adiabatic coupling. Due to the small magnitude, however, it is not a significant cause of decoherence.

The evolution of the above-defined overlaps for the studied case can be seen in panel (b) of Figure 3.7, along with the degree of coherence. We can see that all inequalities (3.12) are satisfied. According to the definitions of the mechanisms of decoherence introduced in Section 1.3, the decrease of $\widetilde{O}_{R,12}$ is considered the second decoherence mechanism – relative motion of the nuclear wave packets on different PECs. The difference between $\widetilde{O}_{R,12}$ and D_{12} would be called the dephasing. In panel (b), we see a lot of "overlap revivals" (the peaks of $\widetilde{O}_{R,12}$), but they do not manifest in coherence revivals. The dephasing somehow compensates for the overlap revivals. We can also notice that the $\widetilde{O}_{P,12}$ behaves similarly as $\widetilde{O}_{R,12}$, only offset in time. This motivates the usage of the square root of their product, which gives a tighter estimate of the degree of coherence. This way, we attributed a part of the dephasing to the relative motion in momentum space.

Panels (c) and (d) of Figure 3.7 show the evolution of the probability densities of the nuclear wave packets populated in the two adiabatic electronic states. The right vertical dashed line serves to check that the first peak of $\widetilde{O}_{R,12}$ indeed corresponds to the moment of crossing of the two nuclear wave packets. The left line denotes the first peak of $\widetilde{O}_{P,12}$. At this moment, both the wave packets are moving in the positive R direction. Both are near the turning point, and have a relatively low momentum.

Let us look at the partial revival at $t \approx 2200\,\text{a.u.}$ Neither the geometric nor the momentum overlap reach the maximal value of 1. This is caused by $\tilde{\chi}_i(R,t)$ being slightly displaced and no more Gaussian. The reason lies in the anharmonicities of the corresponding PECs. Those are visible in panel (a) of Figure 3.6. The effect is more pronounced for $\tilde{\chi}_1(R,t)$, whose corresponding PEC seems "more anharmonic;" there is a plateau at $-1\,\text{a.u.} \lesssim R \lesssim 0\,\text{a.u.}$

This case exhibits initially coherent behaviour, followed by fast decoherence. The reason for the suppression of early-time decoherence is the PECs being parallel at the Franck-Condon point, as we discussed in Section 1.3.1. We compared the degree of coherence with the overlaps of amplitudes of the nuclear wave packets in position and momentum representations. We have seen that both these overlaps must be significant to allow for significant coherence. We have also seen a strong partial revival of coherence.

3.2.2 Variable energy offset of one well

Let us move to the case of E_L carrying the R-dependence of the coupling potential. The definition of the model is in the caption and panels (a)–(d) of Figure 3.8. We see an avoided crossing of the adiabatic PECs. Since the R-dependence of the electronic Hamiltonian is given by an energy offset of one of the wells, the R-dependence of the adiabatic states is insignificant when not close to the avoided crossing. When passing through the crossing, the two corresponding states delocalize and then switch positions (see panels (b)–(d)). Thanks to this, the strictly diabatic states are a good approximation to the diabatic states obtained via the diabatic transformation. We will use the diabatic separation of the density matrix and populate an equal-weight superposition of the strictly

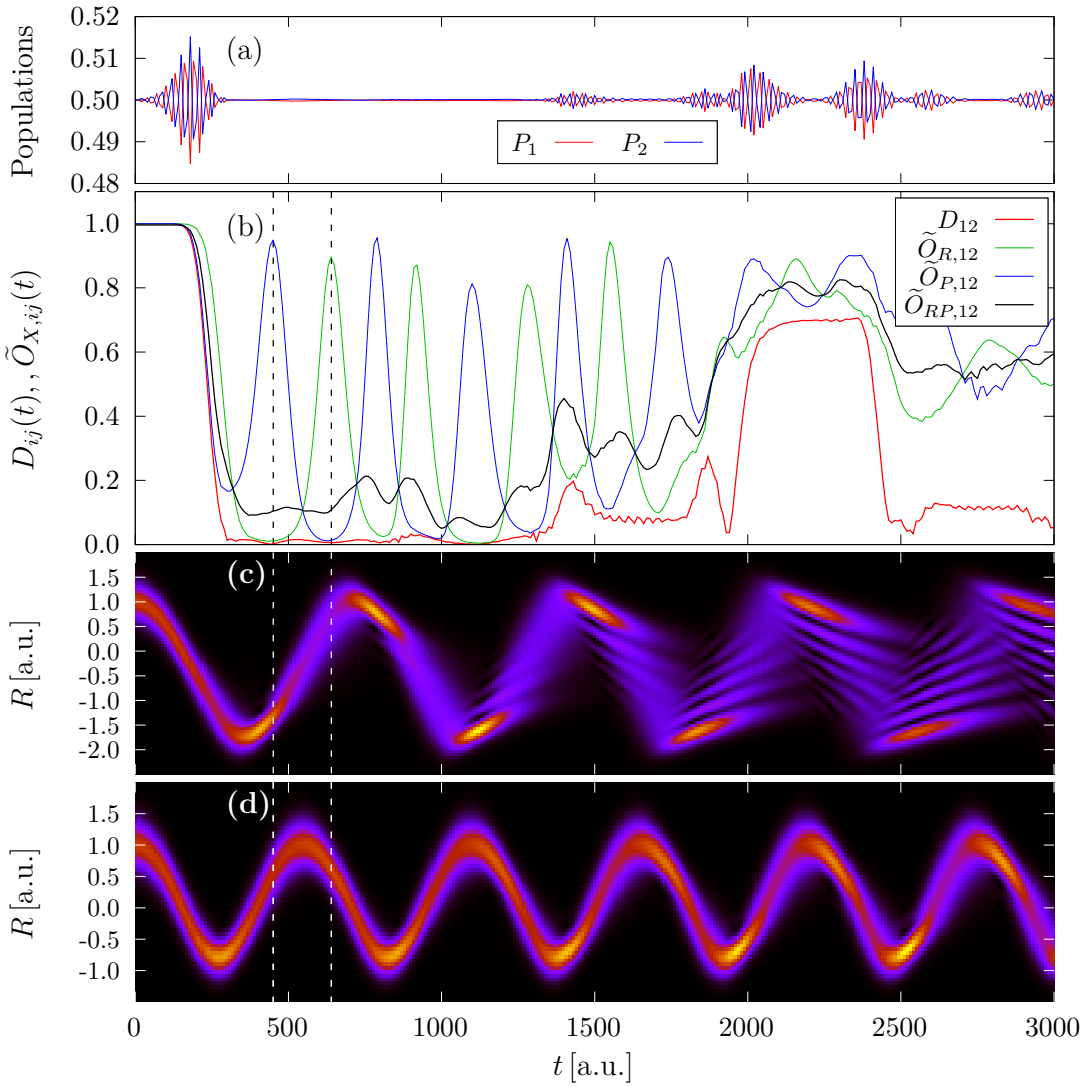

Figure 3.7: (a) Evolution of populations. (b) Evolution of the degree of coherence and the overlaps. (c)–(d) The evolution of the probability densities corresponding to the two nuclear wave packets $\chi_1(R,t)$ and $\chi_2(R,t)$ present in the first and second adiabatic states.

diabatic states. The nuclear wave packet will be populated at $R \approx 1$ a.u.

In panel (e), we can observe the population dynamics caused by the couplings of the diabatic states. The difference $|P_1 - P_2|$ maximizes (within the plotted interval) at $t \approx 380$ a.u. at the value of ≈ 0.2. Panel (f) shows the evolution of the measures of coherence. After an initial decoherence, we observe two revivals: at $t \approx 90$ a.u. and $t \approx 280$ a.u. They do not seem to correlate with the behaviour of the populations. In panels (g) and (h), we can see the evolution of the electronic and nuclear densities. At the initial time and the time of the second (and more pronounced) revival, we can see the coherent oscillations of the electronic density. When the system is in a statistical mixture, the electronic density directly corresponds to the population of the states. For example, at $t \approx 380$ a.u., the density is significantly larger in the right well centered around $R = 2$ a.u. Looking at panel (d), we see that the strictly diabatic state located in this well is $\psi_1(r)$, and its population $P_1 \approx 0.6$ is larger at the considered time. The evolution of nuclear density is complicated and could be described as corresponding to several wave packets moving on each of the two diabatic PECs, generated at different times and with different momenta via the non-adiabatic transfer between the electronic states.

In Figure 3.9, we can see a more detailed look at the population dynamics, the comparison of the degree of coherence D_{12} with the overlaps $\widetilde{O}_{X,12}$, and the momentum space probability density of the nuclear wave packets occupying the two diabatic states. We can see that the early-time decoherence is caused by what we defined as the third decoherence mechanism – the dephasing. This behaviour has been predicted for actual molecules in Ref. [9]. More precisely, it can be attributed to the decrease in momentum overlap $\widetilde{O}_{P,12}$. It describes decoherence correctly up to $t \approx 40$ a.u. We can also attribute the first revival to a realignment of the wave packets in the momentum space. In the second revival, a dominant role is played by the dephasing effects not connected with the momentum overlap.

Let us now comment on the reason for the increase in momentum overlap at the time of the first revival. Panels (c) and (d) in Figure 3.9 showing the probability densities in momentum space will be handy. The nuclear wave packets start moving toward the crossing from the initial position. The upper diabatic PEC has a more steep slope, its wave packet $\chi_2(R,t)$, therefore, reaches the crossing earlier, and the couplings cause part of the wave packet to move onto the other PEC. From the population dynamics, we can see that, indeed, in this first stage $P_2(t)$ decreases. It occurs at $t \approx 65$ a.u., marked by the left dashed vertical line. At this time, the nuclear density of $\widehat{\chi}_1(P,t)$ starts to "emerge" at $P \approx -25$ a.u. This momentum is slightly lower than the momentum of the density corresponding to $\widehat{\chi}_2(P,t)$ – the wave packet lost some momentum during the transition to the other state. The momentum of the transferred part of $\widehat{\chi}_1(P,t)$ is closer to the momentum of $\widehat{\chi}_2(P,t)$ than the momentum of the original part of $\widehat{\chi}_1(P,t)$; therefore, this transfer increases the momentum overlap. The same effect applies slightly later, when $\widehat{\chi}_1(P,t)$ arrives at the crossing, and a part of it transfers into $\widehat{\chi}_2(P,t)$. Both these transitions increase the momentum overlap until it peaks at $t \approx 80$ a.u., denoted by the right vertical dashed line. The following momentum overlap decrease has the same cause as the original one – relative motion of the two nuclear wave packets on different PECs.

In this case, we have seen the evolution of nuclear wave packets on two cross-

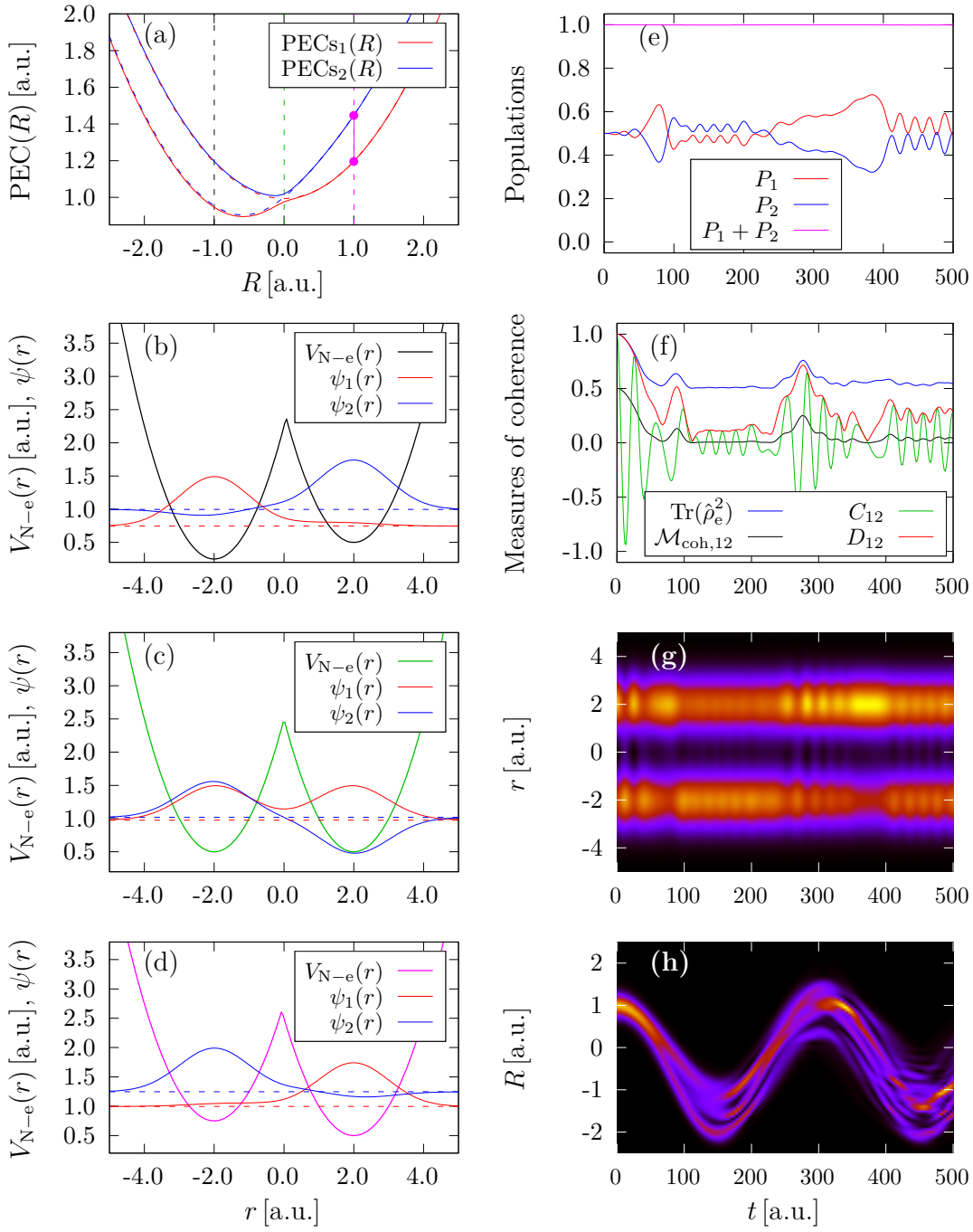

Figure 3.8: (a) Adiabatic (solid lines) and diabatic (dashed lines) PECs for a model with the following parameters (in atomic units): $R_0 = 0$, $\omega_{\mathrm{N}} = 0.02$, $m = 1000$, $E_{\mathrm{N}} = 0$, $r_0 = 4$, $\omega_{\mathrm{L}} = 1$, $\omega_{\mathrm{R}} = 1$, $E_{\mathrm{L,min}} = 0$, $E_{\mathrm{L,max}} = 1$, $a_{E_{\mathrm{L}}} = 1$, and $E_{\mathrm{R}} = 0.5$. The magenta dots indicate the initial state whose evolution we study – coherent superposition (of strictly diabatic states at $\widetilde{R} = 1\,\mathrm{a.u.}$) with equal weights $1/\sqrt{2}$ was populated. Strictly diabatic separation is used. The black, green, and magenta dashed lines indicate the geometries at which the R-cuts of the electronic adiabatic states in panels (b), (c), and (d), respectively, are calculated. (e) Evolution of populations of the first two strictly diabatic states and their sum. (f) Evolution of the measures of coherence of the system. (g) Evolution of the electronic density $\rho(r, t)$. (h) Evolution of the nuclear density $\rho(R, t)$.

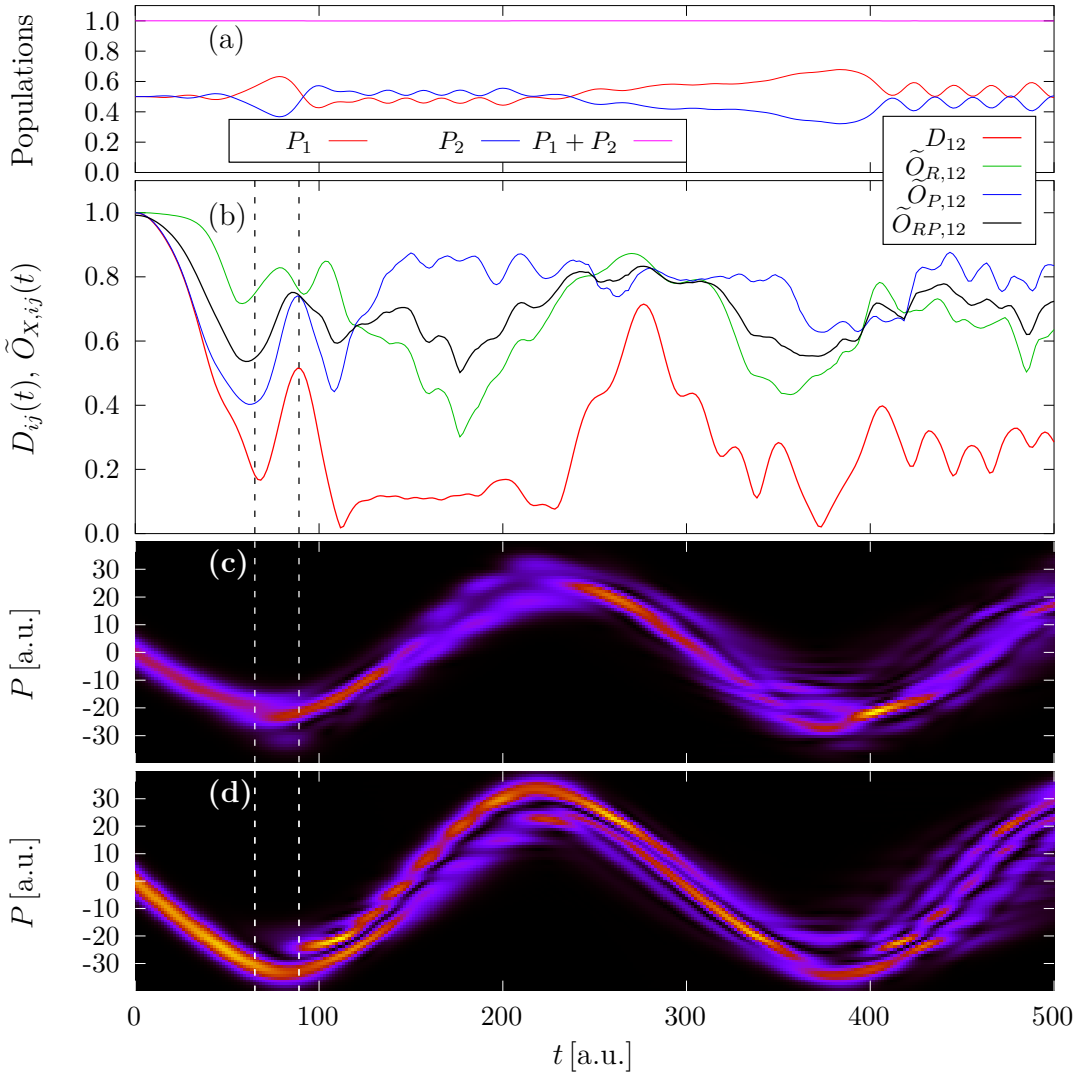

Figure 3.9: (a) Evolution of populations. (b) Evolution of the degree of coherence and the overlaps. (c)–(d) The evolution of the probability densities corresponding to the two nuclear wave packets in the momentum representation $\widehat{\tilde{\chi}}_1(P,t)$ and $\widehat{\tilde{\chi}}_2(P,t)$, respectively, present in the first and second diabatic states.

ing diabatic PECs. We observed population dynamics. We interpreted the first coherence revival using the coupling of the PECs but not the population dynamics itself. We have also seen that in the early-time decoherence is caused by the dephasing mechanism, more specifically, the relative motion of nuclear wave packets in momentum space.

3.2.3 Variable width of one well

The last fundamental case of coupled electron-nuclear dynamics is defined by the R-dependent width of one of the wells. The specific values of the variables are in the caption of Figure 3.10. The PECs and two R-cuts of the coupling potential $V_{\mathrm{N-e}}(r, R)$ with the corresponding strictly diabatic states are shown in panels (a)–(c) of Figure 3.10. We are varying the width of the left well. Its adiabatic state is slightly R-dependent which results in a small difference between the corresponding adiabatic and diabatic PEC. We use the adiabatic separation and populate an equal-weight superposition of adiabatic states with the nuclear wave packet centered at $R = 1\,\mathrm{a.u.}$

In panels (d) and (e), we can see the evolution of the coherence measures. We observe gradual decoherence with periodic dampened partial revivals. The oscillations of *electronic coherence* C_{12} change their frequency. It is visible in panel (e) that at the initial time and the time of the first revival $t \approx 300\,\mathrm{a.u.}$ the frequency is smaller than in the local minimum of C_{12} at $t \approx 150\,\mathrm{a.u.}$ This change in frequency is also visible in panel (f), which shows the evolution of the electronic density. The reason is the varying energy gap between the two PECs. The larger the energy gap, the faster the oscillations. At the initial time and at the time of the first revival, both nuclear wave packets are at their right classical turning point (see panel (g) of Figure 3.10), where the energy gap is the smallest. Conversely, at the time of the first local minimum of coherence, the nuclear wave packets are at their left turning point, where the energy gap is the largest. Moreover, the left turning point is slightly offset for the two PECs, which is the primary cause of decoherence.

In Figure 3.11, we can see the evolution of the two nuclear wave packets' populations, overlaps, and probability densities. As expected, populations remain within a 1 % margin at their initial values. As mentioned above, there are two features to the degree of coherence evolution. We hinted that the periodic decoherence and revivals could be attributed to the offset of the left classical turning points of the PECs. This is well visible for the first period of this behaviour. In panel (b), we can see that the minimum of the degree of coherence occurs when the geometric overlap is minimal. The momentum overlap is, at that time, maximal, reaching almost the value of 1. Both wave packets are standing still (changing the direction of motion), but they are at different positions (see panels (c) and (d)). All revivals happen when the nuclear wave packets are around their initial position, and all coherence minima happen when both are around the opposite turning point.

Another interesting feature is the gradual decrease of coherence and damping of the revivals. We will show that this is caused by different periods of motion of the nuclear wave packets on their PECs. The nuclear wave packets are reaching the turning points at increasingly different times. Therefore, when they "meet"

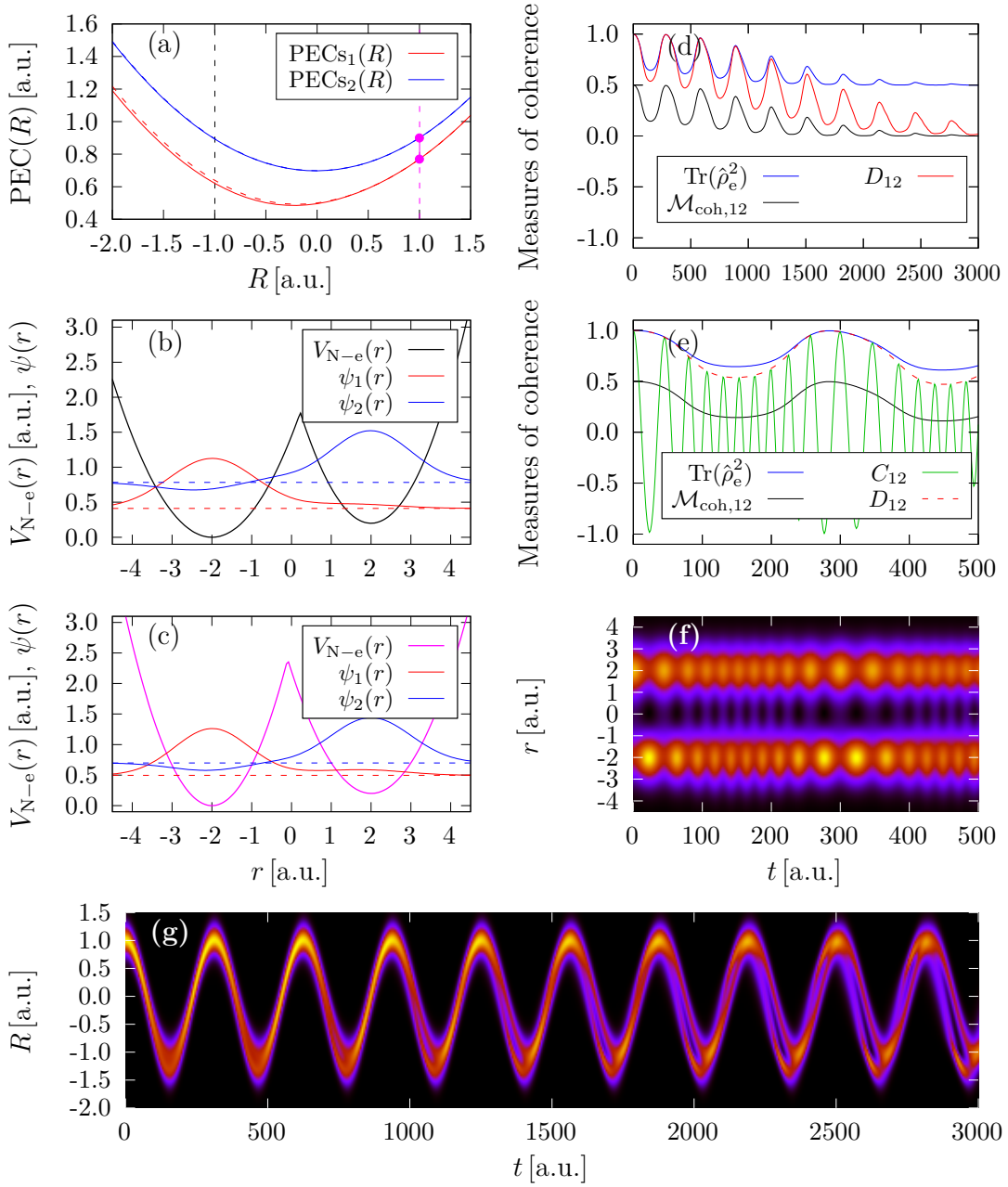

Figure 3.10: (a) Adiabatic (solid lines) and diabatic (dashed lines) PECs for a model with the following parameters (in atomic units): $R_0 = 0$, $\omega_{\mathrm{N}} = 0.02$, $m = 1000$, $E_{\mathrm{N}} = 0$, $r_0 = 4$, $\omega_{\mathrm{L,min}} = 0.7$, $\omega_{\mathrm{L,max}} = 1.3$, $a_{\omega_{\mathrm{L}}} = 1$, $\omega_{\mathrm{R}} = 1$, $E_{\mathrm{L}} = 0$, and $E_{\mathrm{R}} = 0.2$. Note that the adiabatic and diabatic PECs are almost identical. The magenta dots indicate the initial state whose evolution we study – a coherent superposition of adiabatic states with equal weights $1/\sqrt{2}$ and the nuclear wave packet at $R = 1$ a.u. Adiabatic separation is used. The black and magenta dashed lines indicate the geometries at which the R-cuts of electronic adiabatic states in panels (b) and (c), respectively, are calculated. (d) Evolution of the measures of coherence of the system. Coherence C_{12} is not shown because its oscillations are too fast for this range on the time axis. (e) A closer look at the initial decoherence and the first revival. (f) Evolution of the electronic density $\rho(r, t)$. (g) Evolution of the nuclear density $\rho(R, t)$.

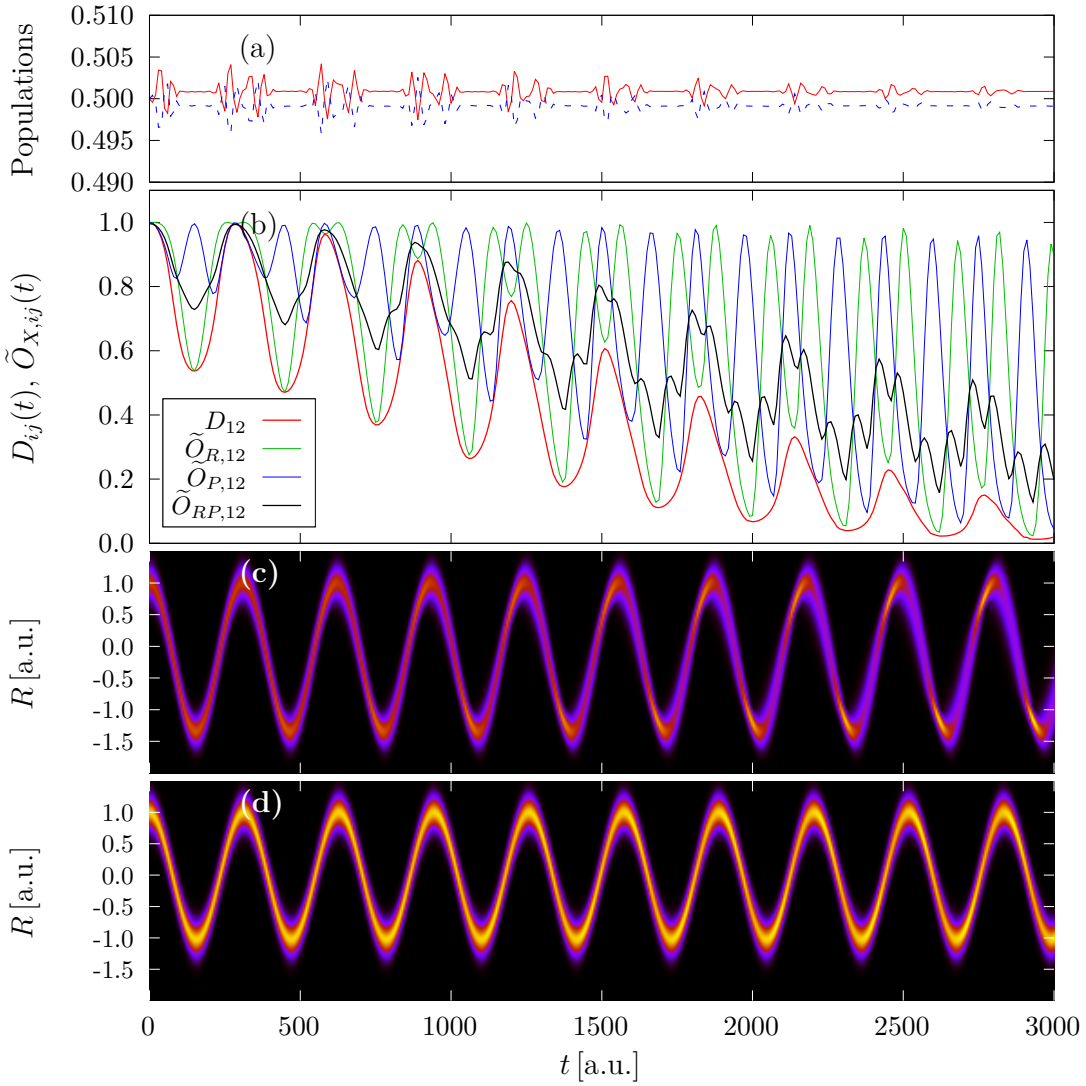

Figure 3.11: (a) Evolution of populations. (b) Evolution of the degree of coherence and the overlaps. (c)–(d) The evolution of the probability densities corresponding to the two nuclear wave packets $\chi_1(R,t)$ and $\chi_2(R,t)$ present in the first and second adiabatic states.

in the position space, they have different momenta (opposite direction of motion) and vice versa. One could call this effect the *dephasing of molecular vibrations*. Notice that the profile of the revivals also changes; the increase in the degree of coherence tends to be faster than the decrease. The reason resides in the evolution of the nuclear wave packet $\chi_1(R,t)$. We see that the probability density tends to peak slightly before reaching the turning point. This is an effect of the anharmonicity of the ground adiabatic PEC caused by the variation of the width of the harmonic well in which the corresponding electronic state resides.

Above, we treated the evolution of geometric and momentum overlaps of nuclear wave packets separately. A valuable tool for combining these two approaches is the *Wigner quasiprobability distribution* (see the original paper in Ref. [20]). It is a phase space function; generally, it is not non-negative, hence the *quasiproba-*

bility attribute. In our context and formalism, it is defined as

$$W_{\mathrm{N}}(R,P,t) = \frac{1}{\pi}\int_{-\infty}^{+\infty} \mathrm{d}R'\, \rho_{\mathrm{N}}(R-R', R+R', t)\, \mathrm{e}^{2iPR'}, \tag{3.13}$$

where $\rho_{\mathrm{N}}(R,R',t)$ is the reduced nuclear density matrix in position representation. Thanks to the orthonormality of adiabatic electronic states, it holds

$$\rho_{\mathrm{N}}(R,R',t) = \sum_i \chi_i(R,t)\chi_i^*(R',t). \tag{3.14}$$

This yields

$$W_{\mathrm{N}}(R,P,t) = \sum_i W_i(R,P,t), \tag{3.15}$$

where $W_i(R,P,t)$ is the time-dependent Wigner distribution corresponding to a pure state $\chi_i(R,t)$. Moreover, the overlap of two states can be expressed as

$$|\,\langle\chi_i(t)|\chi_j(t)\rangle\,|^2 = 2\pi\int_{-\infty}^{+\infty}\mathrm{d}R\int_{-\infty}^{+\infty}\mathrm{d}P\, W_i(R,P,t)W_j(R,P,t). \tag{3.16}$$

Recall that

$$\langle\chi_i(t)|\chi_i(t)\rangle = P_i(t). \tag{3.17}$$

The Wigner distribution corresponding to a normalized state $\chi_i(R,t)$ is then

$$\widetilde{W}_i(R,P,t) = \frac{1}{P_i(t)}\, W_i(R,P,t). \tag{3.18}$$

Finally, it follows that

$$D_{ij}^2 = 2\pi\int_{-\infty}^{+\infty}\mathrm{d}R\int_{-\infty}^{+\infty}\mathrm{d}P\,\widetilde{W}_i(R,P,t)\widetilde{W}_j(R,P,t). \tag{3.19}$$

The phase space overlap of the Wigner distributions of the normalized nuclear wave packets is the square of the degree of coherence between two corresponding electronic states. In this paragraph, we used the adiabatic representation. Analogous formulae hold in the diabatic representation as well.

We can now return to the evolution of the studied case. Figure 3.12 shows six snapshots of the evolution of the Wigner distribution of the nuclear wave packet. In the top panels, the times correspond to the initial state and maxima of two revivals. The bottom panels show the consequent minima of D_{ij}. The two contours indicate the positions of Wigner distributions of the two individual nuclear wave packets. We can see all of the above-discussed behaviour. The initial decoherence is caused by the offset of the left turning point of the two PECs. We can see that the degree of coherence minimizes before the nuclear wave packets reach their turning points – their momenta are still negative.

As time progresses, the nuclear wave packet corresponding to $\chi_1(R,t)$ gets ahead of the other in terms of the accumulated phase by its phase space trajectory (note that the way our phase space axes are oriented, the motion is counter-clockwise). This decreases the overlap of the two Wigner distributions. Above, we called this effect the *dephasing of molecular vibrations*. Furthermore, we observe

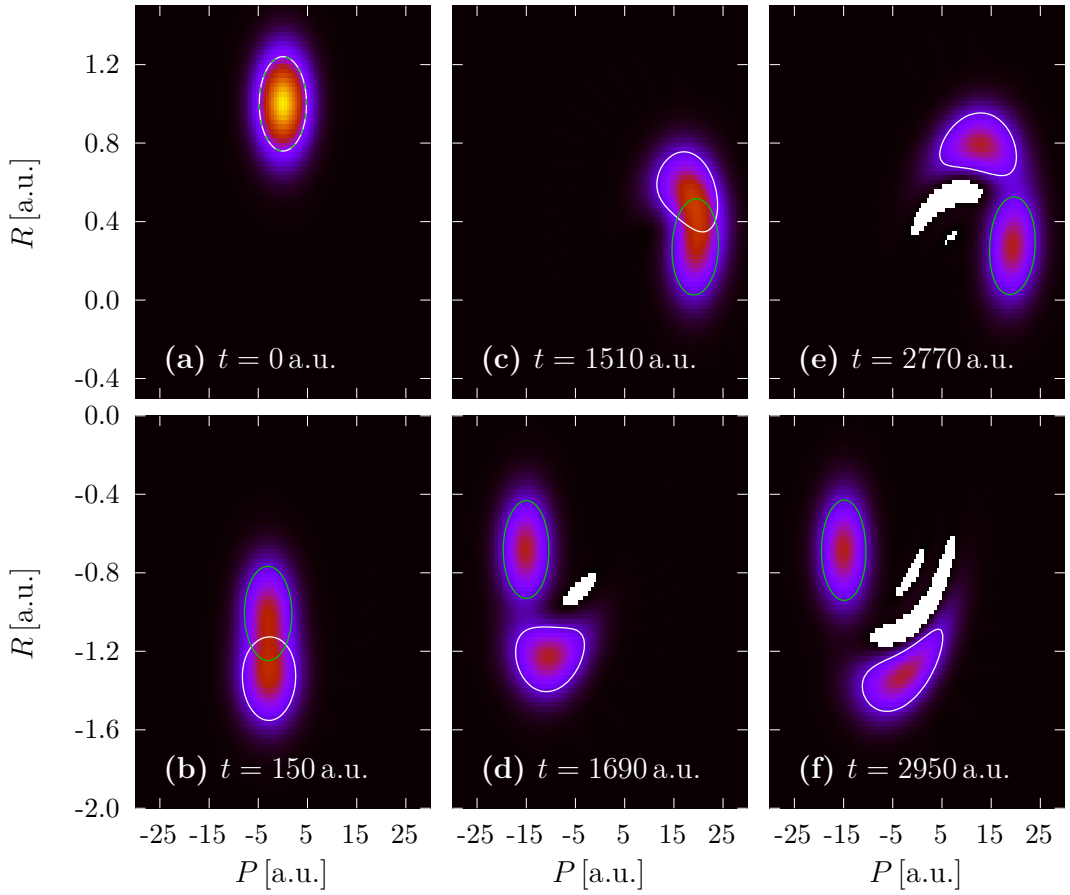

Figure 3.12: Snapshots of the evolution of the Wigner quasiprobability distribution of the reduced nuclear density matrix. The regions where the distribution is negative are shown in white. The white and green contours indicate the isolines of the Wigner distributions corresponding to the individual nuclear wave packets $\chi_1(R,t)$ and $\chi_2(R,t)$, respectively.

that the Wigner distribution of the wave packet $\chi_1(R,t)$ with time progressively deviates from the initial Gaussian shape. We even see the appearance of regions of negative values of the Wigner distribution.

To summarize, we have seen a case with periodic, gradually dampened revivals. We used the geometric and momentum overlaps to interpret the decoherence mechanism. We also demonstrated the power of the Wigner distribution to visualize and better understand the nature of the dephasing mechanism.

3.3 The normal modes of the H_2O^+ cation

In this final section, we present our model's approximation of H_2O^+ and compare it with the previously published study of decoherence in this cation. The water molecule has three normal vibrational modes: the *asymmetric stretch*, the *symmetric stretch*, and the *bending mode*, with the corresponding frequencies [12] $\omega = 3756\,\mathrm{cm}^{-1}$, $\omega = 3657\,\mathrm{cm}^{-1}$, and $\omega = 1595\,\mathrm{cm}^{-1}$, respectively.

In Ref. [12], the authors study the evolution of an initial superposition of the four lowest electronic states up to $t = 5\,\mathrm{fs}$[1]. They treated the normal modes separately and found that the electronic subsystem remains coherent for the asymmetric stretch; its purity does not drop below 0.9. The symmetric stretch causes the purity to drop immediately to $\approx 2/3$ at $t \approx 1\,\mathrm{fs}$. A slow increase of purity follows until it peaks at the value of ≈ 0.95 at $t \approx 4\,\mathrm{fs}$. After that, purity drops similarly as at the beginning. Finally, the bending mode causes purity to drop to $\approx 1/2$ within the first femtosecond, from where it slowly decreases to $1/4$, which it reaches at $t \approx 5\,\mathrm{fs}$.

For simplicity, we will use only the first three electronic states. The *ab initio* PECs of the three normal modes of vibrations of the water cation are shown in panels (a)–(c) of Figure 3.13. They were calculated using cc-pVTZ basis [21] on the O and both H atoms. The ground state of the neutral molecule was calculated using the second-order many-body perturbation theory (MBPT2), as it is implemented in the `MOLCAS` software [22]. A second-order algebraic diagrammatic construction, ADC(2)x [23], was used to calculate the H_2O^+ potentials [24].

We fitted the parameters of the nuclear potential $V_\mathrm{N}(R)$ to the *ab initio* PECs of the ground state of the neutral molecule. The parameters of the coupling potential $V_{\mathrm{N-e}}(r,R)$ were fitted so that the first three adiabatic PECs resemble the *ab initio* ones as best as possible. Due to the large number of parameters and their complicated relationship with the PECs (through numerical matrix diagonalization), this fitting was done "by hand." The parameters used for the individual modes are summarized in Table 3.1. The approximations of individual modes within our model are shown in Figure 3.13 as well. We use the adiabatic separation and adiabatic electronic states in the initial superposition.

Panel (d) shows the evolution of electronic purity yielded by the model. We immediately see that the evolution qualitatively fits the one from Ref. [12] with three fundamental differences. First, our "incoherent" value of purity is $1/3$ – of course, we used three electronic states instead of four (and the evolution does not populate any more states). The second significant difference is that our model seems to have "rescaled" the time by a factor of two. It may be caused by

[1] For clarity, we will use *femtoseconds* as well in this section.

our model being very simple and our approximations of the PECs being crude (especially for the symmetric stretch). On the other hand, in Ref. [12], a harmonic approximation of the *ab initio* PECs at the Franck-Condon point is used for the nuclear dynamics performed using the multiconfiguration time-dependent Hartree method (MCTDH). This is also a rather crude approximation, especially at later times, when the nuclear wave packets are no longer in the Franck-Condon region. The third difference is that we obtained a small revival of purity for the bending mode between $t \approx 7\,\mathrm{fs}$ and $t \approx 12\,\mathrm{fs}$. We will return to this last issue later.

There are other minor differences. Our approximation of the asymmetric stretch preserves purity at the maximal value almost exactly. We obtained a complete revival for the symmetric stretch instead of a partial one (but still significant) seen in Ref. [12]. However, concerning the simplicity of our model and the fact that we used only three electronic states instead of four, we consider obtaining the qualitative agreement to be more than acceptable.

Now, let us briefly discuss the decoherence mechanisms that play a role in the evolution of the above-described approximation of the normal modes. First, the asymmetric stretch does not decohere at all. The Franck-Condon point is at the equilibrium of all three PECs; the nuclear wave packet stays at the initial position. The PECs are not non-adiabatically coupled, so the populations also remain unchanged.

The PECs of the symmetric stretch are not non-adiabatically coupled either. Their main feature (both *ab initio* and model) is that the first two are parallel with each other, while the third is not. Thus, the first two states should remain coherent while the third should decohere and become a statistical admixture. We see that the value of the purity in the first minimum at $t \approx 4\,\mathrm{fs}$ is $\approx 2/3$. The purity of a statistical mixture of two states with populations $P_1 = 2/3$, $P_2 = 1/3$ is $5/9$. Panel (a) of Figure 3.14 shows a snapshot of the Wigner distribution at $t = 4\,\mathrm{fs}$. Positions of the wave packets in individual electronic states are highlighted. Indeed, the nuclear wave packets in the first two states (the white and green isolines) are relatively close together, while the third (the blue isoline) is further away.

Finally, let us comment on the fastest decohering case – the bending mode. The reason for the abrupt decrease of purity is evident from the shape of the PECs. We expect vastly different dynamics of the three nuclear wave packets: $\chi_1(R,t)$ is in the vicinity of the equilibrium of its PEC, it will move slowly to the left; $\chi_2(R,t)$ will move rapidly to the right; and $\chi_3(R,t)$ will move to the left, faster than $\chi_1(R,t)$. A snapshot of the Wigner distribution at $t = 5\,\mathrm{fs}$ is shown in panel (b) Figure 3.14. It documents the discussed relative motion of the wave packets.

The evolution of the nuclear density is shown in panel (c). The contributions of the three nuclear wave packets can be distinguished by the direction and velocity of their movement and the positions of their turning points. The white horizontal line marks the position of the crossing of the second and third PECs. We can see that $\chi_3(R,t)$ crosses it and then returns. The population dynamics can be seen in panel (d) of Figure 3.14. The sum of populations of the first three electronic states remains at the value of 1 within the margin of 2 %. The population of the third state partially migrates to the second one. This occurs from $t \approx 5\,\mathrm{fs}$ and peaks at $t = 9.5\,\mathrm{fs}$. This correlates with the partial purity revival. The purity of

a system occupied by n states with populations P_i has a minimal value of $\sum_{i=1}^{n} P_i^2$ if the states are incoherently mixed. This lower estimate of the purity is plotted in panel (d) of Figure 3.13 with the magenta dashed line. We have found the cause of the partial revival of purity in our model of the bending mode.

Let us now address the reason for the population dynamics. Panels (e) and (f) of Figure 3.14 show how the adiabatic states differ on the two sides of the crossing. We see that $\psi_2(r)$ and $\psi_3(r)$ are switching their roles. Note that since our electronic Hamiltonian is one-parametric (R), its PECs can never actually cross; all crossings are avoided. When the nuclear wave packet $\chi_3(R,t)$ reaches the point of the crossing, the corresponding electronic state is located in the right well. When it advances further left, the electronic state does not change its shape; it remains in the right well, causing the "name" of the electronic state to change to $|\psi_2\rangle$, effectively changing the nuclear wave packet to $\chi_2(R,t)$. The non-adiabatic coupling is such that the nuclear wave packet moves on its *diabatic* PEC without "feeling" any effect of the other one.

What happens in a real H_2O^+ cation? Table 3.2 describes the symmetry of the water cation and its electronic states. We see that the second and third electronic states along the bending mode cut of their PESs have different symmetries. Therefore, they are not non-adiabatically coupled and cross each other[2]. This is the reason for the partial revival not appearing in Ref. [12]. In our model, the dynamics was essentially correct, but it "switched" the meaning of two PECs in a certain part of the R-space, which resulted in an artificial revival. Using the diabatic separation fixes this problem; see the black dashed line in panel (d) of Figure 3.13.

Table 3.1: Specification of parameters of the potentials $V_{\mathrm{N}}(R)$ and $V_{\mathrm{N-e}}(r,T)$ that approximate the normal modes of vibrations of the H_2O^+ cation. If a single value is given, the parameter has a fixed value. If a range and one more number are given, the parameter is R-dependent according to (2.40), the range specifies $f_{\min}$ and $f_{\max}$, and the additional number is the value of the parameter a. All values are given in atomic units. In all cases: $R_0 = 0$ and $m = 1836$.

The parameter	Asymmetric stretch	Symmetric stretch	Bending
ω_{N}	0.0180	0.0175	0.0075
E_{N}	−76.33	−76.33	−76.33
r_0	0.0–12.0, 0.1	12.0	12.0
ω_{L}	0.24	0.20–0.40, −1.0	0.10–0.38, 0.5
ω_{R}	0.24	0.40	0.26
E_{L}	0.29–0.34, −0.2	−0.75–1.25, −0.3	0.31
E_{R}	0.36–0.42, 0.1	−0.71–1.29, −0.3	0.31–0.51, −1.5

[2]The states could actually be coupled via the asymmetric stretch, which reduces the symmetry to C_s, where the reduction of both A_1 and B_2 is A'.

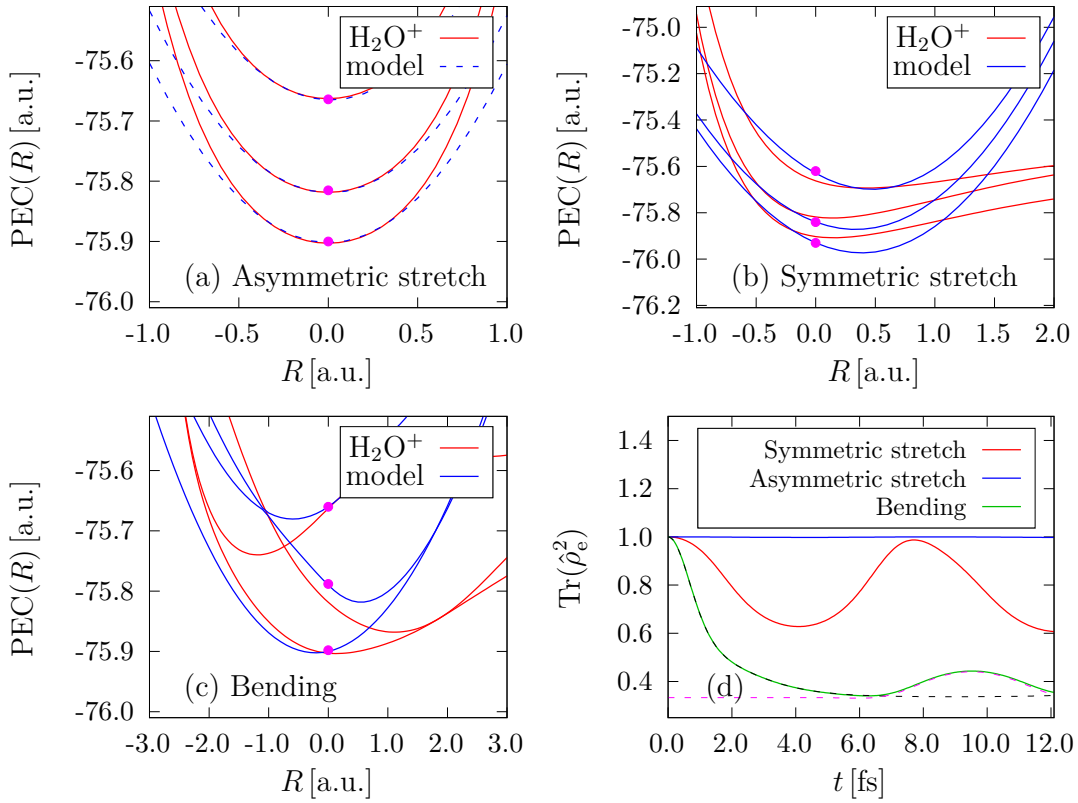

Figure 3.13: Cuts of the PESs of H_2O^+ cation along the normal mode coordinates: (a) asymmetric stretch, (b) symmetric stretch, and (c) bending mode. The panels also show the adiabatic PECs of the model that approximate the *ab initio* ones. The magenta dots indicate the initial state – an equal-weight superposition of the three lowest electronic states at the Franck-Condon geometry. We populate a wave packet corresponding to the ground state of the used nuclear potential $V_N(R)$, approximating the ground vibrational state of the neutral H_2O molecule for the concerning normal mode. Adiabatic separation and adiabatic electronic states are used. Panel (d) shows the evolution of purity in our model. The magenta line denotes $\sum_{i=1}^{3} P_i^2$ (see text for details). The black dashed line shows the purity evolution in the bending mode model with diabatic separation. Note that we use femtoseconds instead of the atomic units of time.

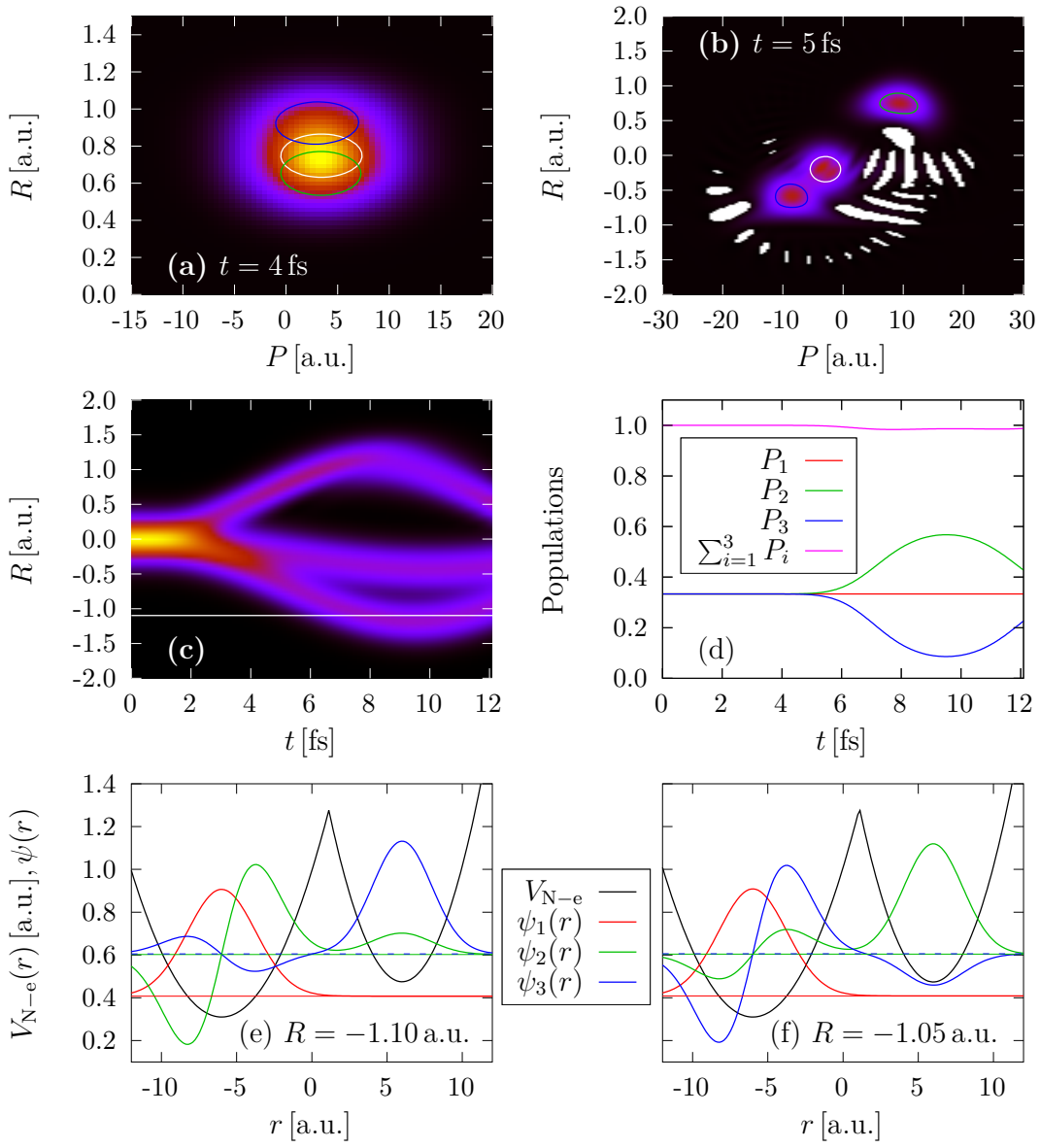

Figure 3.14: The Wigner distribution of the nuclear part of the wave function in our approximation of (a) the symmetric stretch at $t = 4\,\mathrm{fs}$ and (b) the bending mode at $t = 5\,\mathrm{fs}$. The white, green, and blue contours indicate the isolines of the Wigner distributions corresponding to the individual nuclear wave packets $\chi_1(R,t)$, $\chi_2(R,t)$, and $\chi_3(R,t)$, respectively. In white are the regions where the Wigner distribution is negative. (c) The evolution of the nuclear density in our approximation of the bending mode. The white line is at the position of the crossing of the second and third PECs. (d) The evolution of populations of the three lowest electronic states in our approximation of the bending mode. The last two panels show R-cuts of the coupling potential $V_{\mathrm{N-e}}(r,R)$ and the first three electronic adiabatic states in the vicinity of the avoided crossing of the second and the third PECs (see Figure 3.13) at (e) $R = -1.10\,\mathrm{a.u.}$ and (f) $R = -1.05\,\mathrm{a.u.}$

Table 3.2: The header shows the three vibrational modes of H_2O^+, whose symmetry point group is C_{2v}. In brackets, the irreducible representation of the normal mode (within C_{2v}) and the general symmetry of the cation upon offsetting the molecule from equilibrium in the direction of the normal mode are given. The table then shows the irreducible representations corresponding to the first three electronic states within the corresponding point groups.

The state	Asym. str. (B_2, C_s)	Sym. str. (A_1, C_{2v})	Bend (A_1, C_{2v})
First	A''	B_1	B_1
Second	A'	A_1	A_1
Third	A'	B_1	B_1

Conclusion

We have constructed a two-dimensional model of coupled electron-nuclear dynamics in molecules based on a harmonic nuclear potential and a combination of two harmonic wells as the potential "felt" by the electrons. The latter depends parametrically on the nuclear coordinate, coupling the two systems together. The model's simplicity enabled a numerically exact solution of the time-independent Schrödinger equation. We used the simple form of the eigenstates' evolution to study the dynamics of an initially coherent superposition of the electronic states. Our goal was to observe the decoherence of the electronic system caused by the coupling to the nuclei and understand the mechanisms that play a role in the process.

In the first chapter, we introduced the theoretical background of the studied phenomena, defined the quantities that measure coherence in the electronic subsystem, and described the mechanisms causing decoherence – the *population dynamics*, the *relative motion of the nuclear wave packets*, and all the other effects are gathered under the term *dephasing*. The second chapter defined the model in detail and described the approach to solving it. The third chapter contains an overview of the coherent results in the case of uncoupled electron and nuclear dynamics, a detailed study of three special cases of the coupled dynamics, and an application of our model to the normal modes of the H_2O^+ cation.

Varying the model's parameters, we simulated qualitatively different situations with different shapes of the system's PECs. This enabled us to demonstrate and study the decoherence mechanisms discussed in the theoretical part. In the case of non-crossing PECs with different periods of oscillations, we demonstrated that the loss of overlap in the momentum space contributes dominantly to the dephasing mechanism. Furthermore, it is responsible for the initial decoherence, which can be suppressed by making the PECs parallel in the Franck-Condon point.

We used the Wigner quasiprobability distribution to visualize the nuclear wave packets in the phase space. It offers valuable insight into the evolution of geometric and momentum overlaps and their interplay. We proposed a new decoherence mechanism, the *dephasing of molecular vibrations*, caused by different periods of motion of the wave packets' Wigner distributions in the phase space. We have also seen that anharmonicities of the PECs cause the wave packets to deviate from their initial Gaussian shape. This also contributes to decoherence.

In the case of strong non-adiabatic coupling, we demonstrated the usefulness of the strictly diabatic states. The couplings of these states enabled coherence revivals by increasing the momentum overlaps by the transfer of the nuclear wave packets between the electronic states.

We have shown that *electronic coherence* C_{ij} is not the most convenient measure of coherence due to its oscillatory behaviour. A more suitable quantity is the *degree of coherence* D_{ij}. It is population-normalized, so it cannot describe *population dynamics*, but it is convenient for the other mechanisms. Both these measures are defined for a combination of two electronic states only. This is fixed by the *electronic purity* $\operatorname{Tr}\hat{\rho}_\mathrm{e}^2$. The purity has its drawback, too, because it is not equivalent to coherence (for details, see Section 1.4). We conclude that the

degree of coherence (when only two electronic states are present) or the purity, combined with time-dependent populations, are the best quantities to fully characterize coherence. We also confirmed the requirement for the two populated electronic states to overlap for the coherent *charge migration* to appear.

Finally, we applied our model to the H_2O^+ cation. We compared our results with Ref. [12]. Qualitatively, we obtained the same behaviour. The asymmetric stretch does not cause electronic decoherence. The symmetric stretch causes partial decoherence and a revival at a later time. The bending mode causes quick, complete decoherence.

The simplicity of the model gives us flexibility in fine-tuning the PECs and the coherent dynamics. An interesting extension could be done by implementing a second dimension for the nuclei. With this, the interplay between the normal modes could be studied.

Bibliography

[1] Michael A. Robb, Andrew J. Jenkins, and Morgane Vacher. Chapter 8 how nuclear motion affects coherent electron dynamics in molecules. In *Attosecond Molecular Dynamics*, Theoretical and Computational Chemistry Series, pages 275–307. The Royal Society of Chemistry, London, 2018.

[2] Claude Cohen-Tannoudji, Bernard Diu, and Franck Laloë. *Quantum Mechanics: Basic Concepts, Tools, and Applications*, volume 1. Wiley-VCH Verlag, Weinheim, 2nd edition, 2019.

[3] Ajit J Thakkar. *Quantum Chemistry (Third Edition)*. IOP Publishing, 2017.

[4] Wenxiang Hu, Bing Gu, and Ignacio Franco. Lessons on electronic decoherence in molecules from exact modeling. *J. Chem. Phys.*, 148:134304, 2018.

[5] Caroline Arnold, Oriol Vendrell, Ralph Welsch, and Robin Santra. Control of nuclear dynamics through conical intersections and electronic coherences. *Phys. Rev. Lett.*, 120:123001, 2018.

[6] Nikolay V. Golubev, Tomislav Begušić, and Jiří Vaníček. On-the-fly ab initio semiclassical evaluation of electronic coherences in polyatomic molecules reveals a simple mechanism of decoherence. *Phys. Rev. Lett.*, 125:083001, 2020.

[7] Gregory A. Fiete and Eric J. Heller. Semiclassical theory of coherence and decoherence. *Phys. Rev. A*, 68:022112, 2003.

[8] Morgane Vacher, Lee Steinberg, Andrew J. Jenkins, Michael J. Bearpark, and Michael A. Robb. Electron dynamics following photoionization: Decoherence due to the nuclear-wave-packet width. *Phys. Rev. A*, 92:040502, 2015.

[9] Morgane Vacher, Michael J. Bearpark, Michael A. Robb, and João Pedro Malhado. Electron dynamics upon ionization of polyatomic molecules: Coupling to quantum nuclear motion and decoherence. *Phys. Rev. Lett.*, 118:083001, 2017.

[10] Danylo T. Matselyukh, Victor Despré, Nikolay V. Golubev, Alexander I. Kuleff, and Hans Jakob Wörner. Decoherence and revival in attosecond charge migration driven by non-adiabatic dynamics. *Nat. Phys.*, 18(10):1206–1213, 2022.

[11] Stefan Pabst, Loren Greenman, Phay J. Ho, David A. Mazziotti, and Robin Santra. Decoherence in attosecond photoionization. *Phys. Rev. Lett.*, 106:053003, 2011.

[12] Caroline Arnold, Oriol Vendrell, and Robin Santra. Electronic decoherence following photoionization: Full quantum-dynamical treatment of the influence of nuclear motion. *Phys. Rev. A*, 95:033425, 2017.

[13] Thomas Gaumnitz, Arohi Jain, Yoann Pertot, Martin Huppert, Inga Jordan, Fernando Ardana-Lamas, and Hans Jakob Wörner. Streaking of 43-attosecond soft-x-ray pulses generated by a passively cep-stable mid-infrared driver. *Opt. Express*, 25(22):27506–27518, 2017.

[14] W. Domcke. *Theorie der Molekülschwingungen und der vibronischen Wechselwirkung*. Vorlesung HHU, Düsseldorf, 1999.

[15] E.B. Wilson, J.C. Decius, and P.C. Cross. *Molecular Vibrations: The Theory of Infrared and Raman Vibrational Spectra*. Molecular Vibrations: The Theory of Infrared and Raman Vibrational Spectra. Dover Publications, New York, 1980.

[16] Frank W. Olver, Daniel W. Lozier, Ronald F. Boisvert, and Charles W. Clark. *NIST Handbook of Mathematical Functions*. Cambridge University Press, USA, 1st edition, 2010.

[17] Milton Abramowitz and Irene A. Stegun. *Handbook of Mathematical Functions with Formulas, Graphs, and Mathematical Tables*. Dover, New York City, 1964.

[18] Per Olov Löwdin. On the non-orthogonality problem connected with the use of atomic wave functions in the theory of molecules and crystals. *J. Chem. Phys.*, 18:365–375, 1950.

[19] J.S.C. Prentice. Composite Gauss–Legendre quadrature with error control. *Int. J. Math. Educ. Sci. Technol.*, 42(4):557–564, 2011.

[20] E. Wigner. On the quantum correction for thermodynamic equilibrium. *Phys. Rev.*, 40:749–759, 1932.

[21] Jr. Dunning, Thom H. Gaussian basis sets for use in correlated molecular calculations. I. The atoms boron through neon and hydrogen. *J. Chem. Phys.*, 90(2):1007–1023, 1989.

[22] Francesco Aquilante, Jochen Autschbach, Alberto Baiardi, Stefano Battaglia, Veniamin A. Borin, Liviu F. Chibotaru, Irene Conti, Luca De Vico, Mickaël Delcey, Ignacio Fdez. Galván, Nicolas Ferré, Leon Freitag, Marco Garavelli, Xuejun Gong, Stefan Knecht, Ernst D. Larsson, Roland Lindh, Marcus Lundberg, Per Åke Malmqvist, Artur Nenov, Jesper Norell, Michael Odelius, Massimo Olivucci, Thomas B. Pedersen, Laura Pedraza-González, Quan M. Phung, Kristine Pierloot, Markus Reiher, Igor Schapiro, Javier Segarra-Martí, Francesco Segatta, Luis Seijo, Saumik Sen, Dumitru-Claudiu Sergentu, Christopher J. Stein, Liviu Ungur, Morgane Vacher, Alessio Valentini, and Valera Veryazov. Modern quantum chemistry with [Open]Molcas. *J. Chem. Phys.*, 152(21), 2020. 214117.

[23] Jochen Schirmer. *Many-Body Methods for Atoms, Molecules and Clusters*, volume 94 of *Lecture Notes in Chemistry*. Springer International Publishing, 2018.

[24] The *ab initio* calculations were performed by Přemysl Kolorenč.